

AD-A110 185

STANFORD UNIV CA EDWARD L GINZTON LAB OF PHYSICS

F/G 11/9

PVF2 TRANSDUCERS FOR NONDESTRUCTIVE EVALUATION OF CERAMICS AND --ETC(U)

OCT 81 D WEINSTEIN, H J SHAW

AFOSR-77-3386

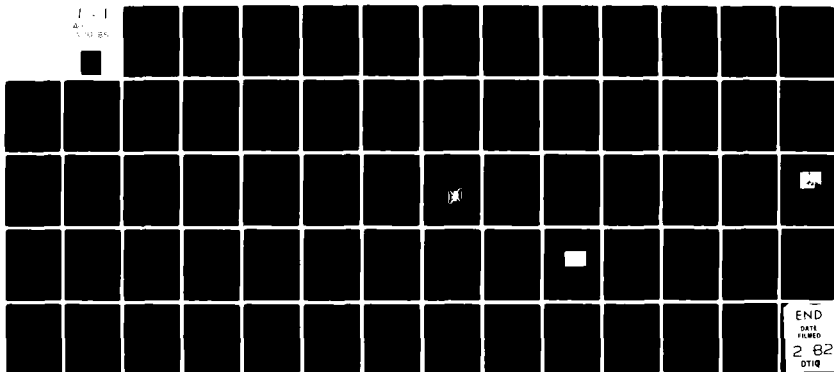
UNCLASSIFIED

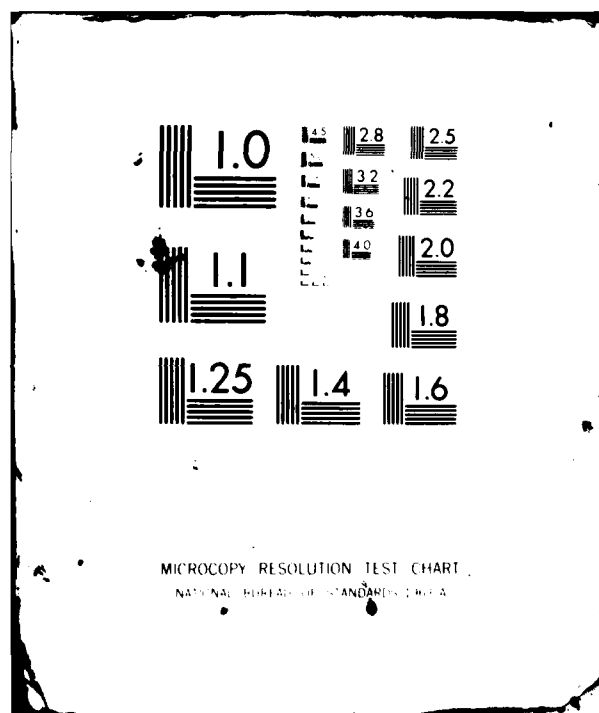
GL-3340

AFOSR-TR-81-08R1

NL

1 - 1  
AD  
5/10/85





UNCLASSIFIED

SECURITY CLASSIFICATION OF THIS PAGE (When Data Entered)

LEVEL 1

(12)

## REPORT DOCUMENTATION PAGE

READ INSTRUCTIONS  
BEFORE COMPLETING FORM

1. REPORT NUMBER

AFOSR-TR- 81 - 0881

2. GOVT ACCESSION NO.

AD-A110185

3. RECIPIENT'S CATALOG NUMBER

4. TITLE (and Subtitle)

PVF<sub>2</sub> TRANSDUCERS FOR NONDESTRUCTIVE EVALUATION  
OF CERAMICS AND BRITTLE MATERIALS

5. TYPE OF REPORT &amp; PERIOD COVERED

Final Report  
7-1-77 through 12-31-80

6. PERFORMING ORG. REPORT NUMBER

G. L. 3340

7. AUTHOR(s)

D. Weinstein and H. J. Shaw

8. CONTRACT OR GRANT NUMBER(s)

AFOSR-77-3386

9. PERFORMING ORGANIZATION NAME AND ADDRESS

Stanford University  
Edward L. Ginzton Laboratory  
Stanford, California 9430510. PROGRAM ELEMENT, PROJECT, TASK  
AREA & WORK UNIT NUMBERS2306-A2  
4110615

11. CONTROLLING OFFICE NAME AND ADDRESS

Air Force Office of Scientific Research  
Building 410  
Bolling AFB, D.C. 20332

12. REPORT DATE

October 1981

13. NUMBER OF PAGES

64

14. MONITORING AGENCY NAME &amp; ADDRESS (if different from Controlling Office)

15. SECURITY CLASS. (of this report)

UNCLASSIFIED

15a. DECLASSIFICATION/DOWNGRADING  
SCHEDULE

16. DISTRIBUTION STATEMENT (of this Report)

Approved for public release; distribution unlimited.

DTIC  
ELECTE

JAN 28 1982

17. DISTRIBUTION STATEMENT (of the abstract entered in Block 20, if different from Report)

B

18. SUPPLEMENTARY NOTES

19. KEY WORDS (Continue on reverse side if necessary and identify by block number)

Polyvinylidene Fluoride (PVF<sub>2</sub>)  
Surface Acoustic Waves  
Wedge Transducers  
Nondestructive TestingPhased Arrays  
Piezoelectric Transducer  
Acoustic Imaging

82 01 28 017

20. ABSTRACT (Continue on reverse side if necessary and identify by block number)

→ An experimental system using PVF<sub>2</sub> piezoelectric film as the active element has been demonstrated which provides electronically-controlled, high speed two-dimensional ultrasonic imaging on the surface of a ceramic sample. Scanning bulk waves are converted to surface waves at the ceramic surface. The system produces an electronically focused, highly convergent surface wave beam with an f/1 aperture, with variable focal length and capable of arbitrary scanning patterns by changing the phase distribution of rf signals applied to a linear array of electrodes via a microcomputer. Simulated flaws on the surface were used in

DD FORM  
1 JAN 73 14731

UNCLASSIFIED

SECURITY CLASSIFICATION OF THIS PAGE (When Data Entered)

AD A110185

DTIC FILE COPY

DTIC FILE COPY



# TABLE OF CONTENTS

	<u>Page</u>
I. INTRODUCTION . . . . .	1
II. SUMMARY OF PVF <sub>2</sub> PIEZOELECTRIC POLYMER PROPERTIES . . . . .	2
A. Introduction . . . . .	2
B. Summary of Structure and Properties of PVF <sub>2</sub> . . . . .	3
III. PVF <sub>2</sub> WEDGE TRANSDUCERS . . . . .	11
A. Introduction to Wedge Transducers . . . . .	11
B. Summary of Wedge Transducer Design . . . . .	13
C. Summary of Surface Wave Pulsed Measurements on SiN Samples . . . . .	19
IV. ULTRASONIC SURFACE WAVE IMAGING ARRAY . . . . .	21
A. Introduction . . . . .	21
B. Introduction to Ultrasonic Imaging . . . . .	23
C. Surface Wave Imaging Approach . . . . .	26
D. Surface Wave Array Design and Construction . . . . .	30
1. Bulk Wave Portion . . . . .	30
2. Surface Wave Portion . . . . .	34
E. Electronic System . . . . .	38
F. Surface Wave Imaging Measurements on Silicon Nitride Samples . . . . .	40
1. System Calibration . . . . .	43
2. Imaging Experiments . . . . .	48
3. Summary and Predictions . . . . .	57
REFERENCES . . . . .	59
APPENDIX - Radiation from a One-Dimensional Transducer Array . . . . .	61

Approved for public release;  
distribution unlimited.

Approved for public release; distribution unlimited.  
This document is the property of the Information Division  
and is loaned to your agency. It and its contents are not to be  
distributed outside your agency.

## I. INTRODUCTION

In most types of device research the progress of the research is heavily dependent on the development of efficient transducers or couplers for coupling energy of one type to energy of another type or for coupling energy in one mode to energy of the same type in another mode. This is very applicable to the field of NDE, where it has been demonstrated in many cases that it is necessary to have efficient transducers in order to be able to detect small flaws, and for the return signals from flaws to have sufficient signal-to-noise ratio to obtain accuracy in the analysis of the flaws. Furthermore, spatial resolution of flaw details is proportional to the bandwidth of the transducers, so that transducer design principles must be developed which make optimum use of the trade-off between conversion efficiency and bandwidth.

Transducers for the excitation of surface acoustic waves (SAW) on ceramic surfaces have been studied in the present program. These include two basic types of transducers and an ultrasonic surface wave imaging array. The two basic types of transducers are the interdigital electrode array and the wedge transducer. The work under the program had several parts. Some of these were described in earlier reports and will not be repeated in this present document. The work on interdigital transducers is described in reference 1, work on the wedge transducer is covered in reference 2, and results on flaw detection in silicon nitride plates using these transducers are given in reference 8. The wedge transducer is also summarized briefly below, as it forms the basis for the work on the surface wave imaging array which is the main subject of this present report.

In the wedge transducer, bulk acoustic waves are first generated and subsequently converted into surface waves at the ceramic surface. Thus a brief summary of ultrasonic bulk wave transducers is included as background material.

All of the transducers and arrays studied are based on  $PVF_2$  piezoelectric film as the active material for converting electrical signals to acoustic signals. A summary of the properties of  $PVF_2$  films relevant to these transducers and arrays is also included below.

## II. SUMMARY OF $PVF_2$ PIEZOELECTRIC POLYMER PROPERTIES

### A. Introduction

In the past decade the use of acoustic waves in nondestructive testing and other fields has increased significantly. Many different types of imaging and probing devices have been constructed. Often, piezoelectric materials have been employed in order to either generate or detect the acoustic waves used to probe the test object. Usually, materials such as PZT (lead zirconate-titanate) or zinc oxide are chosen as the piezoelectric material.

Many other types of solid materials such as quartz, bone, tendons and wood also exhibit piezoelectricity. In nearly all cases, however, this piezoelectricity is extremely weak. But in 1969 Kawai<sup>3</sup> showed that the synthetic polymer polyvinylidene fluoride ( $PVF_2$ ) is strongly piezoelectric compared to other polymers. Piezoelectrically active  $PVF_2$  is in the form of thin sheets,  $PVF_2$  has a piezoelectric strength of the same order of magnitude as crystalline quartz.

Among the strong piezoelectrics  $PVF_2$  has a unique set of properties. It is flexible and can be made to conform to desired shapes. Very thin films (down to the order of several microns) have prospects for use as

transducers at frequencies above 40 MHz.  $\text{PVF}_2$  also has a low acoustic impedance, close to that of water and very different from those of the common piezoelectric materials. This is a very important characteristic in regard to acoustic devices as will be seen.

$\text{PVF}_2$  has already found commercial applications for which some of its properties appear to be unique, leading to simpler designs, less expensive implementation and improved performance. Among these are piezoelectric membranes for the construction of high quality, inexpensive audio components, and dielectric layers for the winding of capacitors for the electronics industry. It is also used as an injection molding medium, as insulation for computer wiring and as inert liners for certain types of storage tanks.  $\text{PVF}_2$  films can also be used as a pressure sensitive element in contactless switches and contactless manual keyboards. There has also been a substantial amount of interest in the use of  $\text{PVF}_2$  films as pyroelectric detectors in infrared imaging.

This document is concerned with the development of  $\text{PVF}_2$  surface wave ultrasonic transducers and surface wave imaging arrays. These devices operate in the 1-20 MHz range, making them suitable for nondestructive testing.

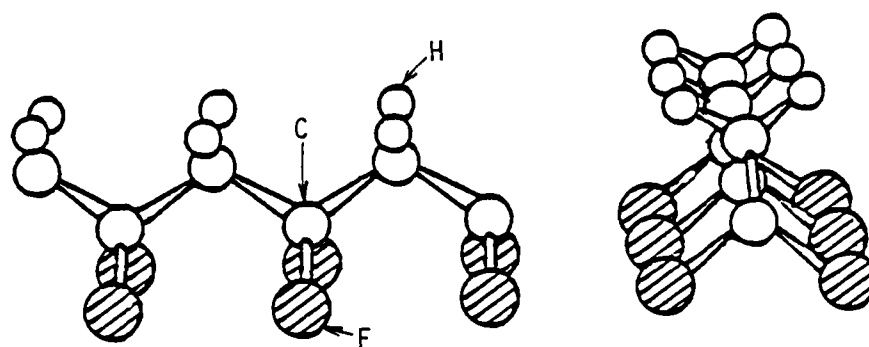
#### B. Summary of Structure and Properties of $\text{PVF}_2$

$\text{PVF}_2$ , being a polymer, consists of long chains which repeat a basic molecular building block many times. The basic building block, or monomer, of  $\text{PVF}_2$  is the group  $-\text{CH}_2-\text{CF}_2$ .

Figure 1 shows part of a  $\text{PVF}_2$  molecular chain. The polymer chain consists of a carbon backbone onto which pairs of alternating hydrogen or fluorine molecules are bonded. Dipole moments exist between the hydrogens



# PLANAR ZIGZAG CONFORMATION



UNIT CELL

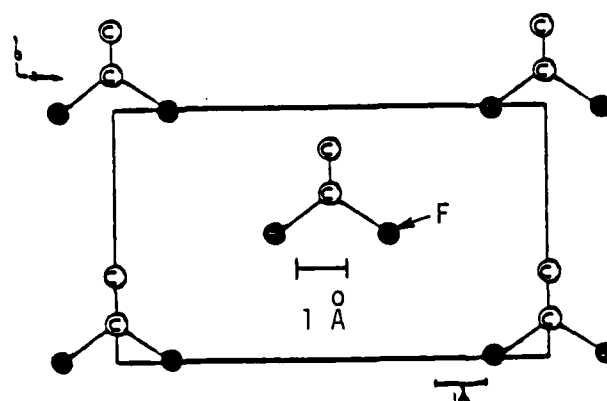


Fig. 1--Top:  $\text{PVF}_2$  beta phase molecular chain. Bottom: End on view of 5 beta phase chains arranged in the unit cell. (Hydrogen atoms not shown for simplicity.)

and the carbons and between the fluorines and the carbons. It is these dipole moments which give  $\text{PVF}_2$  most of its piezoelectricity.

In a bulk sample of  $\text{PVF}_2$  an individual chain can take many forms and shapes. These various forms occur because the carbon backbone can twist and turn into a wide variety of stable states. There are also numerous ways in which these chains can be aligned with regard to one another. There are at least three possible crystalline phases - alpha, beta, and gamma, as well as an amorphous phase. These phases differ from each other in both the structures of their chains and the way these chains are arranged to form the crystal structure.

The beta phase has a higher piezoelectric constant than any other phase. The chain shown in Fig. 1 is a beta phase chain. The figure also shows (from an end on view) the arrangement of these chains in a unit cell of beta  $\text{PVF}_2$ . Beta phase  $\text{PVF}_2$  belongs to the crystalline symmetry class orthorhombic  $2mm$ . Unfortunately, when  $\text{PVF}_2$  is crystallized from the melt under standard laboratory conditions, the alpha phase is preferentially formed. Alpha phase film can be converted into the more active beta film by uniaxially stretching the  $\text{PVF}_2$ . This forces an untangling of any twisted molecular chains which are present, as well as a phase change. The film is generally increased in length by a factor of 3-5 during this process. Following this procedure the film is then poled in order to rotate and align the dipole moments all in the same direction. Poling fields are on the order of 80 volts/micron. The poling field is applied perpendicular to the film surface. This is usually defined as the  $z$  coordinate direction, while the stretching direction is taken as the  $x$  axis.

Since PZT-5A is a commonly used piezoelectric ceramic it is interesting and useful to compare its properties to those of  $\text{PVF}_2$ . The physical properties of  $\text{PVF}_2$  are listed in Table I along with those of PZT-5A.

One very important difference is the piezoelectric strength of the two materials. Two of the values listed in Table I involve piezoelectric strength. One is a component of the piezoelectric stress constant tensor,  $e(z3)$ . The complete  $e$  tensor appears in the piezoelectric constitutive relations:

$$\underline{T} = - \underline{e} \cdot \underline{E} + \underline{C}^E \cdot \underline{S} \quad (1)$$

$$\underline{D} = \underline{\epsilon}^S \cdot \underline{E} + \underline{e} \cdot \underline{S} \quad (2)$$

where  $\underline{T}$  is a  $6 \times 1$  stress tensor,

$\underline{S}$  is a  $6 \times 1$  strain tensor,

$\underline{E}$  is the electric field vector ( $3 \times 1$ )

$\underline{D}$  is the displacement vector ( $3 \times 1$ )

$\underline{C}^E$  is the elastic stiffness matrix at zero  $\underline{E}$  field ( $6 \times 6$ )

$\underline{\epsilon}^S$  is the dielectric matrix at zero strain ( $3 \times 3$ )

$\underline{e}$  is the piezoelectric stress constant matrix ( $6 \times 3$ ).

If all components of  $\underline{e}$  are zero, Eqs. (1) and (2) reduce to two separate and uncoupled equations, one relating stress to strain, and the other relating  $\underline{D}$  to  $\underline{E}$ . Thus, the larger the magnitude of  $\underline{e}$ , the greater the coupling between elastic and electrical effects.

Because  $\text{PVF}_2$  has a crystal symmetry of the class orthorhombic  $2mm$ , symmetry arguments require that the  $\underline{e}$  tensor of  $\text{PVF}_2$  must have the following form:

TABLE I

	<u>PVF<sub>2</sub></u>	<u>PZT-5A</u>
Density (gm/cm <sup>3</sup> )	1.78	7.75
Stiffened acoustic (m/sec) velocity	2150	4350
Elastic constant (N/m <sup>2</sup> ) $c_{33}^E$	$9 \times 10^9$	$11.1 \times 10^{10}$
Acoustic impedance (kg/m <sup>2</sup> - S) $\times 10^6$	3.82	33.7
Relative dielectric constant, ( $\epsilon_{zz}^S/\epsilon_0$ )	8	830
Piezoelectric stress constant $e_{z3}$ (c/m <sup>2</sup> )	- .08 to - .165	15.8
Electromechanical coupling constant	.01 to .04	.31

$$e = \begin{matrix} & 0 & 0 & 0 & 0 & e_{15} & 0 \\ 0 & 0 & 0 & 0 & e_{24} & 0 & 0 \\ e_{31} & e_{32} & e_{33} & 0 & 0 & 0 & 0 \end{matrix}$$

The most important component of the  $e$  tensor is  $e_{33}$ . Remember that the  $z$  direction is defined parallel to the poling direction or, equivalently, perpendicular to the surface of the  $PVF_2$  film. All the devices reported on here use the  $e_{33}$  component of the tensor. Although the other components of the tensor are often relevant to the operation of some acoustic devices, none of them are relevant to the particular devices described in this document.

Table I gives a value of  $e_{33}$  between  $-.08$  coulombs/m<sup>2</sup> and  $.165$  coulombs/m<sup>2</sup> for  $PVF_2$ . The lower value best fits the characteristics of our  $PVF_2$  devices. However, Ohigashi has reported larger values of  $e_{33}$  up to  $-.165$  C/m<sup>2</sup>.<sup>4</sup> These differences may be due to variations in the processing parameters used in the fabrication of the  $PVF_2$  samples tested.

A quantity which gives a better measure of the acoustic insertion loss of a transducer is the dimensionless electromechanical coupling coefficient  $k_t^2$ .  $k_t^2(33)$  is defined by the equation:

$$k_t^2(33) = e_{33}^2 / (C_{33} \cdot \epsilon_{33})$$

where  $C_{33}$  is a component of the elastic stiffness matrix that appears in Eq. (1), and  $\epsilon_{33}$  is a component of the dielectric constant matrix that appears in Eq. (2).

$k_t^2$  can often be used as a figure of merit. It can be defined in terms of energy in the following manner. Assume a transducer has electrodes covering the faces which are perpendicular to the  $z$  direction. Further assume

that the thickness of the transducer in the  $z$  direction is small compared to the lateral size of the transducer. When an electric field parallel to the  $z$  direction is used to drive the transducer,  $k_t^2(33)$  is approximately the ratio of the stored electrical energy in the piezoelectric to the stored elastic energy.

It is also a good measure of the acoustic insertion loss of an electrically driven piezoelectric, since the output of a transducer is often proportional to  $k_t^2$ , rather than  $e_{(33)}$ . Table I lists the values of  $k_t^2$  for  $\text{PVF}_2$  and PZT. A range of values is given corresponding to the range of  $e_{(33)}$  values mentioned above.  $\text{PVF}_2$  is about an order of magnitude weaker than PZT-5A in this regard.

The lower value of  $k_t^2$  is a negative tradeoff in the use of  $\text{PVF}_2$ . However, the acoustic impedance of  $\text{PVF}_2$  (3.82) is much lower than that of PZT-5A (34.3). When operating into a low impedance load such an impedance is a distinct advantage since it minimizes reflections at the load-transducer interface. This, in turn allows large frequency bandwidths and a clean impulse response without resorting to matching layers. This fact is important because our wedge transducers operate into load materials which have impedances quite close to that of  $\text{PVF}_2$ , such as lucite or silicone rubbers. Although we have not done so, others have used water as a convenient wedge material.<sup>5</sup> As water has an impedance of only 1.48, the benefits of  $\text{PVF}_2$  listed above extend to wedge transducers using water wedges.

Additionally, it has been shown that  $\text{PVF}_2$  can stand much higher applied driving electric fields than PZT. Thus the weaker piezoelectric strength of  $\text{PVF}_2$  relative to PZT can be compensated by using higher applied fields when driving  $\text{PVF}_2$  devices.<sup>6,7</sup>

Futhermore,  $\text{PVF}_2$  is thin and flexible while PZT is hard and difficult to work with in thin layers. Thus  $\text{PVF}_2$  can conform to simple curved shapes if conditions demand such flexibility. Very thin films (on the order of 5 microns) have the prospect for use as fundamental mode transducers at frequencies near 90 MHz. Earlier work has shown that piezoelectric activity in  $\text{PVF}_2$  persists up to 500 MHz.<sup>8</sup> In contrast to these figures, PZT is rarely used as an acoustic transducer above 10 MHz because of difficulties in working with the very thin and brittle PZT plates required to achieve resonant frequencies above 10 MHz.

The  $\text{PVF}_2$  used in this work was obtained through two sources. The larger amount was supplied by Kureha Corp. of Japan. The Kureha  $\text{PVF}_2$  was either 9 or 25 microns thick, and was uniformly electroded on both sides with an aluminum film of approximately 500 angstroms when received. The  $\text{PVF}_2$  had been poled in the z direction and uniaxially stretched. We removed the aluminum film, substituted other film, and repoled the samples before use, as described later. We also obtained poled and stretched samples of  $\text{PVF}_2$  film fabricated in the Stanford Center for Materials Research thorough the work of R. Feigelson, R. Route and R. DeMattei. The samples produced by CMR ranged in thickness from 12 to 45 microns.

### III. $\text{PVF}_2$ WEDGE TRANSDUCERS

#### A. Introduction to Wedge Transducers

In this section we summarize some of the design and operating principles of surface wave wedge transducers relevant to the design of the imaging array of Section IV.

A surface wave differs from a bulk plane wave in several respects. A bulk wave traveling in a homogenous material is not subject to any boundary conditions until it encounters a surface. However, a surface wave traveling at a plane boundary between a substrate and air will have to satisfy the boundary condition that the stress at the air interface equals zero. This forces the surface wave to behave somewhat differently than a bulk wave in terms of particle displacement, stress, wave velocity and strain.

A surface wave wedge transducer excites a surface wave by insonifying a surface with a bulk plane wave. The angle of incidence is chosen so that the wave fronts of the incident wave will phase match to a surface wave on the substrate. This says that the equation

$$\sin\theta = \frac{V_2}{V_S} \quad (3)$$

is satisfied, where  $V_2$  = bulk wave velocity in material 1 and  $V_S$  surface wave velocity on the substrate. Figure 2 is a diagram of the physical set-up.

The specific material parameters of both the wedge and substrate determine the coupling conversion strength between the bulk and surface waves. As the surface wave travels to the right in Fig. 2 its amplitude increases due to the continual radiation of the bulk wave onto the substrate. But the



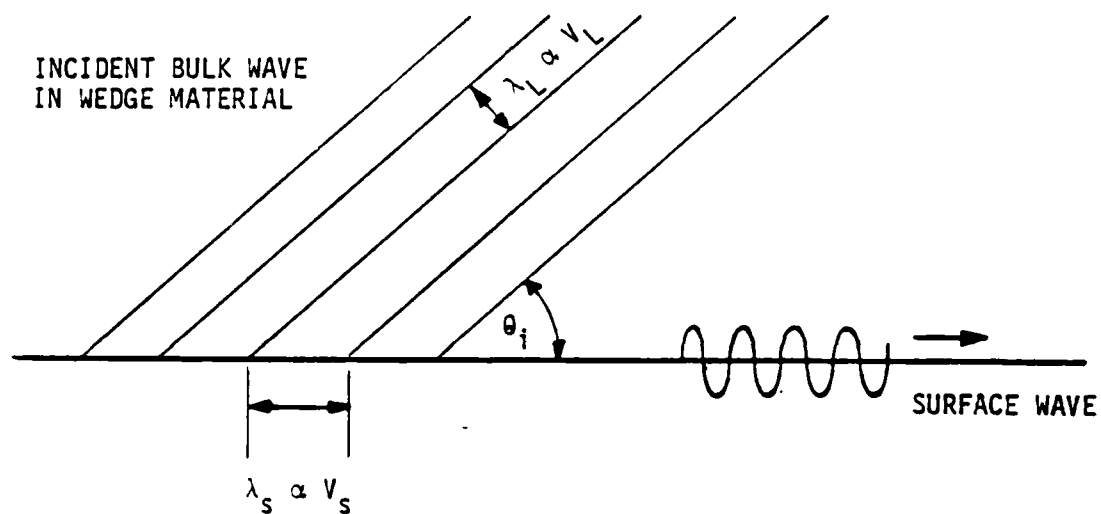


Fig. 2--Incident bulk wave coupling to a surface wave.  
 $\lambda_L$ ,  $V_L$  = longitudinal wavelnegth and velocity.  
 $\lambda_S$ ,  $V_S$  = surface wavelnegth and velocity.

traveling surface wave also can and will re-radiate energy back to the wedge material in the form of a bulk wave. It has been shown by Fraser et al.<sup>9</sup> that there is an optimum coupling length to use in order to excite a surface wave with maximum possible efficiency relative to the bulk wave transducer radiating into the wedge. This length depends on the material parameters of the wedge and the substrate, including the surface wave velocity on the substrate, the substrate density, the longitudinal wave impedance of the wedge and the bulk wave attenuation constant of the wedge. In designing a wedge transducer one calculates two principal quantities, namely an angle of incidence and an optimum coupling length, using the parameters listed above.

#### B. Summary of Wedge Transducer Design

In designing wedge transducers, the substrate material is quite important, since the design parameters depend on the substrate properties, as explained above. We chose to use silicon nitride ( $\text{Si}_3\text{N}_4$ ) as the test material. Silicon nitride is a strong, brittle, light ceramic that is currently of great interest to the manufacturers of aircraft and automobiles. The properties of this ceramic are such that it may be superior to metals in the construction of many expensive machine parts.

We have previously constructed  $\text{PVF}_2$  surface wave transducers<sup>2</sup> of the type shown in Fig. 3. In this model we used a wedge made of RTV 615, a silicone rubber. The wedge angle was 10 degrees and the coupling length was 7 mm at 18 MHz. (The frequency is specified because the coupling length is inversely proportional to frequency.) The  $\text{PVF}_2$  is brassbacked and radiates bulk waves into the RTV.

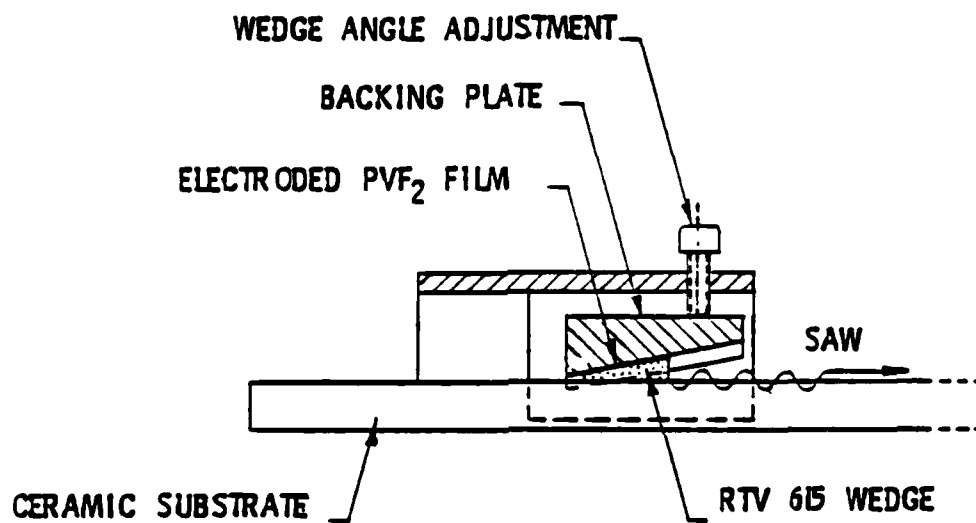


Fig. 3--PVF<sub>2</sub> wedge transducer, side view.

Because this type of surface wave transducer relies on a bulk wave transducer as the source of acoustic energy, we will now discuss some elementary aspects of bulk wave transducers.

Practical ultrasonic bulk wave transducers often approximate plane layered structures, consisting of a piezoelectric layer plus matching layers, backing material and load material. Figure 4 shows such a device. When a voltage is applied across the piezoelectric layer, acoustic waves are radiated through any intervening matching layers present, into the load and backing materials.

If the applied voltage is sinusoidal in time, the power radiated by the transducer will depend on the frequency of the driving voltage. At a particular frequency, usually referred to as the resonant frequency, the power radiated into the load material will be a maximum. Most transducers using piezoelectric ceramics (such as lead zirconate titanium-PZT) will deliver maximum power to the load, or resonate, when the piezoelectric layer has a thickness equal to  $\lambda/2$ , where  $\lambda$  is the acoustic wavelength in the piezoelectric. This occurs because the ceramics have high acoustic impedances and thus are usually bounded by lower impedance materials when used in transducers. The phase shifts which occur when acoustic waves are reflected off the boundaries result in the  $\lambda/2$  resonant condition mentioned above.

The shape of the resonant power peak as a function of frequency also depends on the relative acoustic impedances of the system. The reflection coefficient,  $R$ , for acoustic wave incident on a plane boundary is

$$R = \frac{Z_2 - Z_1}{Z_2 + Z_1} \quad (4)$$

# TRANSDUCER WITH MATCHING LAYERS

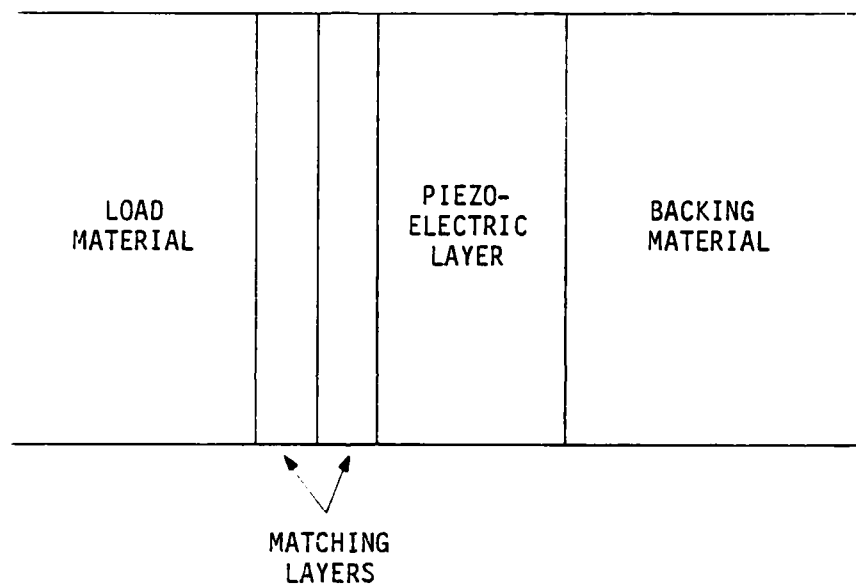


Fig. 4--Layered transducer schematic.

where  $Z_1$  and  $Z_2$  are the acoustic impedances of the reflecting material and the propagation material, respectively. The closer the impedance match between the two materials, the less the reflection. Ceramic transducers have an impedance of  $\sim 34 \times 10^6 \text{ kg/m}^2\text{s}$ , while the most common and convenient load materials in our wedge transducers have low ( $\sim 3$ ) impedances. Therefore, waves attempting to leave the ceramic and enter the wedge are highly reflected. This causes complex reverberations in the ceramic leading to (1) a very sharp resonant power peak, i.e., narrow bandwidth when operated with cw or long tone pulse excitation, (2) poor impulse response when operated with short pulses, and (3) inefficient power transfer even at the resonant frequency. For these reasons, matching layers of intermediate impedances are generally placed between the ceramic and the water.

Currently, most PZT transducers employ matching layers in order to increase the transducer efficiency. These matching layers have an acoustic impedance lying between those of the load and the PZT-5A. The effect of these layers is to reduce the impedance mismatch between the PZT and the load. For instance, a half inch diameter PZT-5A transducer with a resonant frequency of 3.5 MHz will typically have a power conversion efficiency of  $\sim 5\%$  when driven from a 50 ohm source. The addition of two carefully chosen matching layers and an electrical matching network between the power source and the transducer will raise the conversion efficiency to  $\sim 60\%$ .<sup>10</sup>

PVF<sub>2</sub> transducers are different from those just described. We construct PVF<sub>2</sub> transducers by bonding electroded PVF<sub>2</sub> film directly to a flat, polished substrate, whose acoustic impedance can be close to that of the PVF<sub>2</sub> film, or much higher than that of the PVF<sub>2</sub> film. The first wedge transducers made here were made with higher impedance backing, and we will briefly describe

these first as they formed the basis for later units, although the latter use nearly matched backings. The high impedance units used brass as backing material. As the acoustic impedance of  $\text{PVF}_2$  is  $\sim 4$  while brass has an impedance of  $\sim 32$ , acoustic reflections at the brass- $\text{PVF}_2$  boundary have an  $180^\circ$  phase shift relative to reflections occurring in transducers using ceramic piezoelectric elements. It turns out therefore, that  $\text{PVF}_2$  transducers resonate in a  $\lambda/4$  thickness mode, not a  $\lambda/2$  mode as is normally the case.

There are other consequences of the low impedance of  $\text{PVF}_2$ . The large impedance mismatch at the brass interface reflects most of the acoustic energy toward the load, where it is needed. The relatively good impedance match between the  $\text{PVF}_2$  and the load results in efficient transfer of acoustic energy and a broadband resonance curve. Also,  $\text{PVF}_2$  transducers radiate a bipolar acoustic wave when excited by a voltage impulse. Such an impulse response is more desirable than the many-cycled ringing impulse response often experienced with piezoelectric ceramics because shorter (in time) transducer impulse responses allow better resolution (in space) when used in time domain reflectometry and acoustic imaging.

The transducer of Fig. 3 consists, in part, of a  $\text{PVF}_2$  brass backed transducer radiating into an RTV load. The  $\text{PVF}_2$  was 25 microns thick and was electroded with about  $50 \text{ \AA}$  of chromium topped by  $1000 \text{ \AA}$  of gold. We removed the aluminum electrodes that were present when we received the film, and evaporated the chromium-gold combination onto both sides of the  $\text{PVF}_2$ . We preferred these new electrodes because they were much more rugged and electrically conductive than the aluminum electrodes.

The transducer resonated near 17 MHz, since this is approximately the quarter wave frequency of 25 micron PVF<sub>2</sub>. However, the frequency dependence of the loss in the RTV lowered the most efficient operating point of the wedge transducer to about 5 MHz. This occurred because the RTV was quite lossy. Its loss as a function of frequency was measured by Fraser, et al.<sup>9</sup> and found to be:

$$\text{loss (dB/cm)} = 1.3 \times F(\text{MHz})^{1.4} \quad (5)$$

This means that at 10 MHz there is a 3.2 dB/mm loss as bulk waves travel through the RTV. Such a loss will severely degrade the magnitude of the surface wave produced on the substrate. As the loss increases as frequency raised to the 1.4 power, the optimum operating frequency of the device is skewed toward lower frequencies.

#### C. Summary of Surface Wave Pulsed Measurements on SiN Samples

The devices described above were used to generate and detect surface acoustic waves on silicon nitride substrates. In one experiment the substrate had three half penny shaped cracks purposely produced on its surface. The location of these flaws is shown in Fig. 5. The flaws were approximately 900 microns in diameter.

In the experiment,<sup>11</sup> the wedge transducer was placed in contact with the ceramic and then driven with a voltage pulse of 300 volts peak magnitude and a width of approximately 100 nanoseconds. This applied voltage generated a surface acoustic wave pulse on the Si<sub>3</sub>N<sub>4</sub>. When the surface wave encountered the flaws, a small portion of the wave was reflected back toward the transducer. At the transducer the reflected pulse was converted back into a detectable electrical signal.



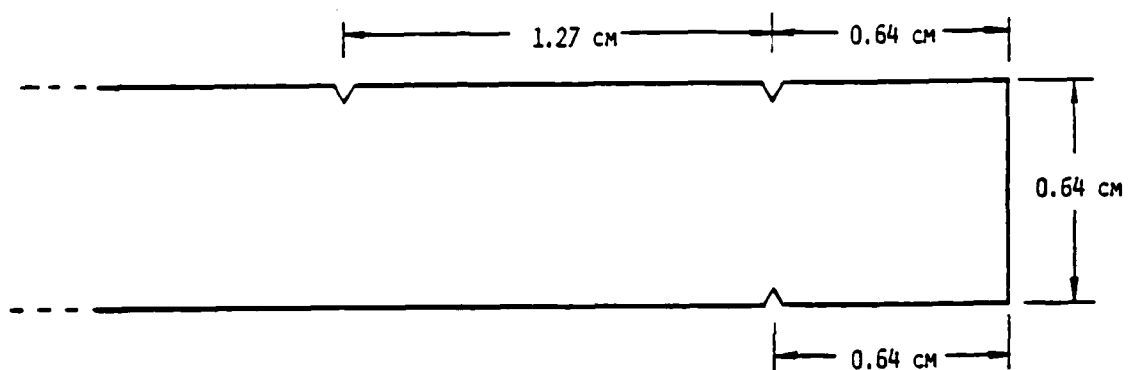


Fig. 5--Location of flaws on ceramic test piece.

This experiment demonstrated the effectiveness of  $\text{PVF}_2$  wedge transducers for use on ceramic substrates. Referring to Fig. 5, with a wedge transducer located to the left of the left-hand flaw on the top surface, the surface wave pulses traveled a distance of approximately 4.2 cm to the most distant flaw, traveling around two intervening sharp corners at one end of the  $\text{Si}_3\text{N}_4$  plate.

We were also able to operate two of these wedge transducers successfully in a pitch-catch mode, but the wedge alignment was a problem. This alignment was critical, and not easily maintained. The design of Fig. 3 allowed the wedge angle to be adjusted to its optimum value experimentally. There was, however, found to be coupling between this adjustment and the transverse position of the wedge on the substrate. It was found that the advantages of the adjustable feature did not outweigh the resulting difficulties in maintaining alignment.

These problems stimulated us to explore new wedge transducer designs. The design changes eliminated all the difficulties just described and resulted in a much better device. These modifications will be described in detail when we consider the design of the  $\text{PVF}_2$  surface wave imaging array.

#### IV. ULTRASONIC SURFACE WAVE IMAGING ARRAY

##### A. Introduction

Currently, the detection of defects in industrial machine parts is of great interest. It would be advantageous to be able to detect and evaluate flaws, and to predict part life.

For example, at the present time ceramic turbine blades are used in high performance areas such as jet engines. The turbine blades are retired from service after a certain operational lifetime because of the high risk

involved in stress failure during operation. All blades past a certain age are retired because it is not possible to differentiate between defective parts and parts which are flawless. This procedure probably wastes many safe and unflawed parts because there is no way to quickly examine the parts for harmful flaws. Thus an effective program of nondestructive testing would be very beneficial.

The defects which must be detected can be divided into two general types - bulk defects and surface defects. Bulk wave defects are typically voids and inclusions. Surface flaws are generally cracks. It has been found that surface cracks are often the starting point for material breakage under stress. On the other hand, voids and inclusions seem to be less detrimental to stressed samples. Therefore, a nondestructive test system that specifically finds surface flaws is of interest at this time.

Ultrasonic waves are being widely studied as a means of detecting flaws. Their wavelengths are in a favorable range for this purpose, and they can be focused into beams of small size for high resolution. Much of this work involves single ultrasonic transducers which are focused and scanned mechanically in probing for flaws. More recently, acoustic imaging methods have received increasing attention because they allow electronic focusing and scanning, which can greatly reduce the time required to examine a given region, which can be a very important cost factor in practical applications.

As part of our research, we have studied a new approach to ultrasonic imaging arrays which allows the formation of electronically scanned and focused surface wave beams on ceramic surfaces. Using thin  $\text{PVF}_2$  polymer films as the active elements, they have future potential for extension to high ultrasonic frequencies for high resolving power. The system is based

on the  $PV\text{F}_2$  wedge surface wave transducers studied earlier under this program.

The work to be presented concerns an adaptation of some general phased array principles to surface waves. Before we turn to the array itself, we will give an overview of general imaging principles as applied to bulk waves, and then describe the conversion to surface waves.

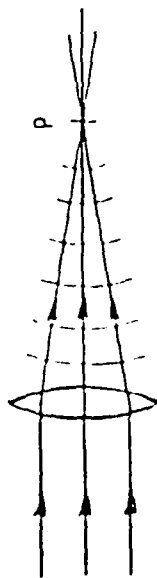
#### B. Introduction to Ultrasonic Imaging

Let us first introduce general ultrasonic imaging of the conventional bulk wave kind, proceeding first from an analogy with optical imaging.

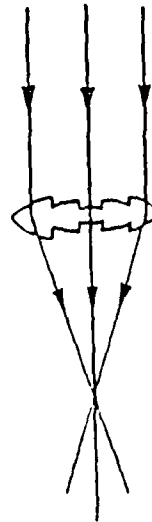
In familiar optical imaging, light from an illuminated object passes through a lens system which produces an image of the object, either enlarged, reduced or unchanged, in some convenient image plane. Light from all points on the object is focused simultaneously onto corresponding points in the image plane. The same could be done with acoustic waves, but it is usually not done this way because, since the image is invisible, further operations are required before the image can be viewed. It usually turns out to be preferable to follow a different procedure from the start, involving scanning across the object.

In the ultrasonic case, scanning acoustic beams are usually used to register each point on the object sequentially, to build up an image point by point. These beams are completely analogous to focused optical beams, and are focused down to a small focal spot by electronic signals applied to arrays of transducers which are functionally equivalent to optical lenses. Let us first look at how these scanning beams are produced, and then discuss how they are used to produce images.

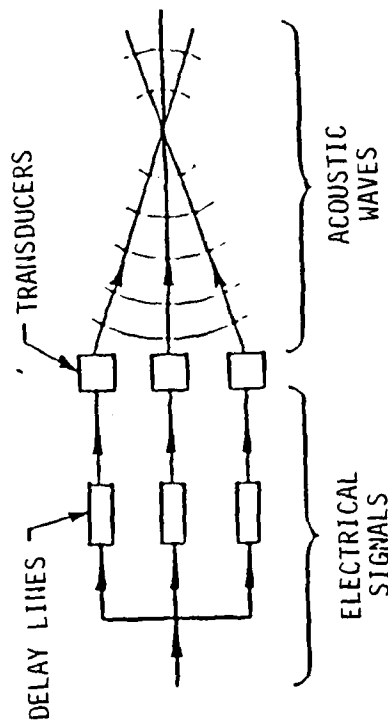
In our system the focused acoustic beam is produced by a phased array. Phased antenna arrays are well known in radar systems where they are used to produce scanning beams in space. These principles can be applied to acoustic transducer arrays, and can be generalized to produce acoustic beams which are electronically focused as well as electronically scanned. The essence of the present system can be seen by considering first the focusing action of a simple lens (Fig. 6(a)). On passing through the lens different light rays experience time delays of different amounts so that at the focal point  $P$  they are all in phase and add to produce an intense spot of small dimensions. This same action can be produced with an array of acoustic transducers (Fig. 6(b)) by inserting delay lines with different time delays in the electrical leads to the transducers, so that the total time delay (electrical plus acoustic) to point  $P$  is the same for all signals. This time delay equalization is a sufficient but not necessary condition for focusing; actually it is only necessary to equalize the phases of the several signals. We can subtract time delays equal to integral numbers of periods of the wave, in a stepped fashion, from the lens of Fig. 6(a), as indicated at (c). We can do the same with the acoustic system as indicated at (d). Here phase shifters, which can shift the phase of electrical signals, are substituted for the delay lines of (b). In the optical lens case (c) there is a disadvantage over the uniform lens case (a) in that spatial quantization noise is introduced; however, this is not the case in the transition from (b) to (d) because both systems use spatially discrete arrays. In the acoustic case, there are substantial advantages in case (d). Phase shifts are simpler to implement than time delays, and can be readily varied by changing the control signals affording electronic control of both focal



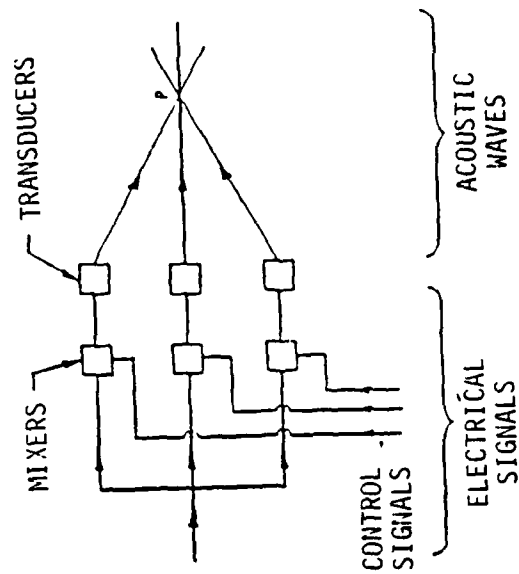
(a) Single lens schematic.



(c) Stepped lens schematic.



(b) Acoustic time delay focusing schematic (three channels shown for illustration; many more are used in practice).



(d) Phased array schematic.

Fig. 6--Illustration of ultrasonic focusing arrangements.

length and beam scanning. This, basically, is the system we are employing. It is equivalent to making small changes in the thicknesses of the various steps in the lens of Fig. 6(c).

### C. Surface Wave Imaging Approach

Our approach to surface wave arrays involves forming a bulk wave imaging array, and converting the bulk waves to surface waves using a wedge. The bulk wave array consists of a  $\text{PVF}_2$  film having an array of parallel electrode fingers on its surface, as indicated in Fig. 7. The details of this array will be given later. For the moment, it is only necessary to view the array as a set of narrow, parallel, closely spaced strips constituting bulk longitudinal-wave transducers. These strip transducers are placed in contact with a material wedge, as indicated in Fig. 7 (a) and (b). In operation, each transducer strip radiates a cylindrical bulk acoustic wave into the wedge, as indicated schematically at (c) for the case of the element labelled C. When this cylindrical wave strikes the surface wave substrate it creates an equivalent surface wave "source" having an axis, indicated by the dashed line labelled I, oriented parallel to the longitudinal axis of the surface wave substrate F. The length of this source covers a substantial number of surface wave wavelengths. The source acts much as an end fire antenna, and radiates a surface wave having wavefronts labelled G in the figure.

In operation, a number of the strips C radiate simultaneously, and their individual waves become superimposed in the wedge material. The instantaneous phases of the rf driving voltages applied to the electrode strips C are individually controlled such that the net field from all the elements is a converging cylindrical wave having wavefronts E (Fig. 7(a) and (b)). These in

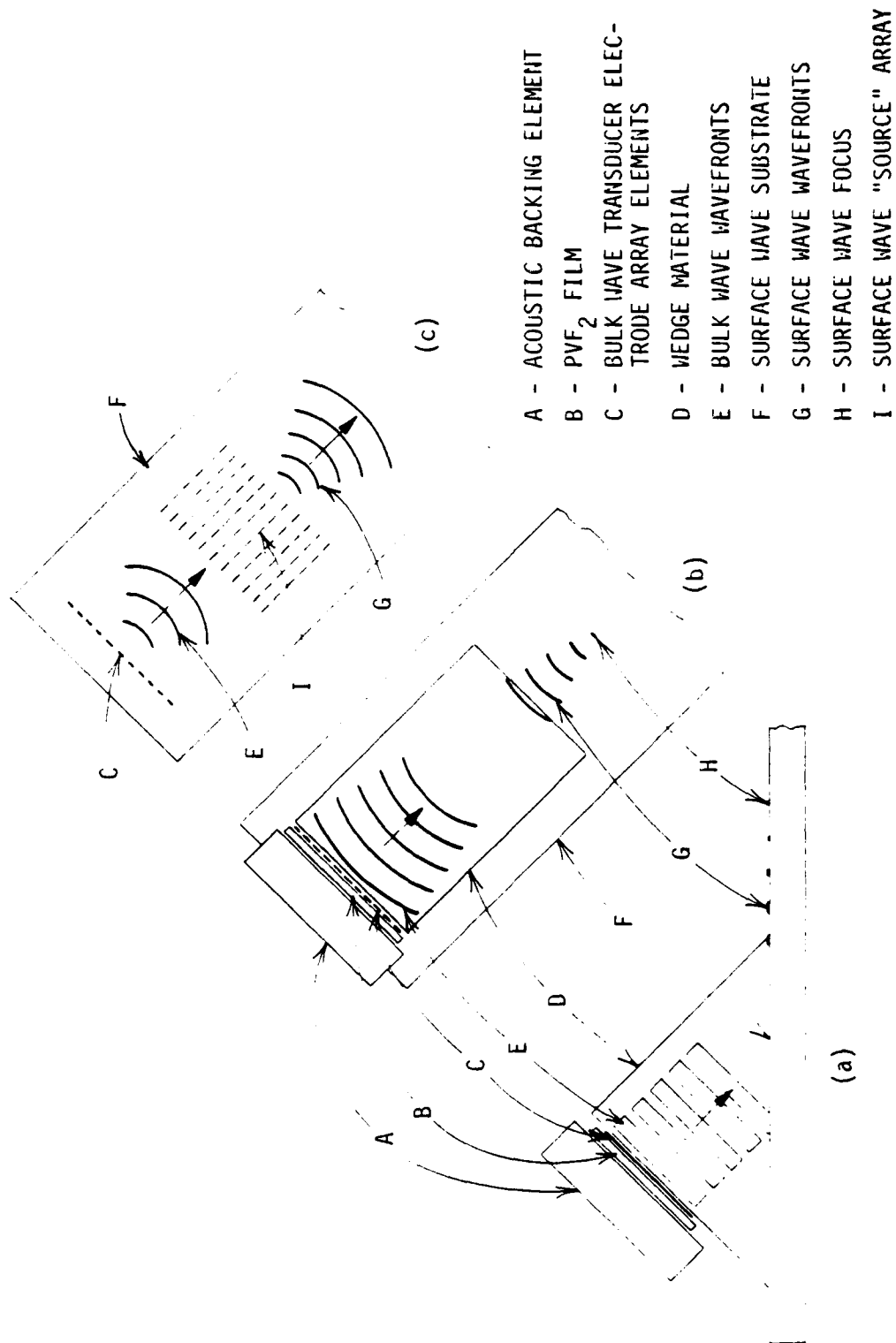


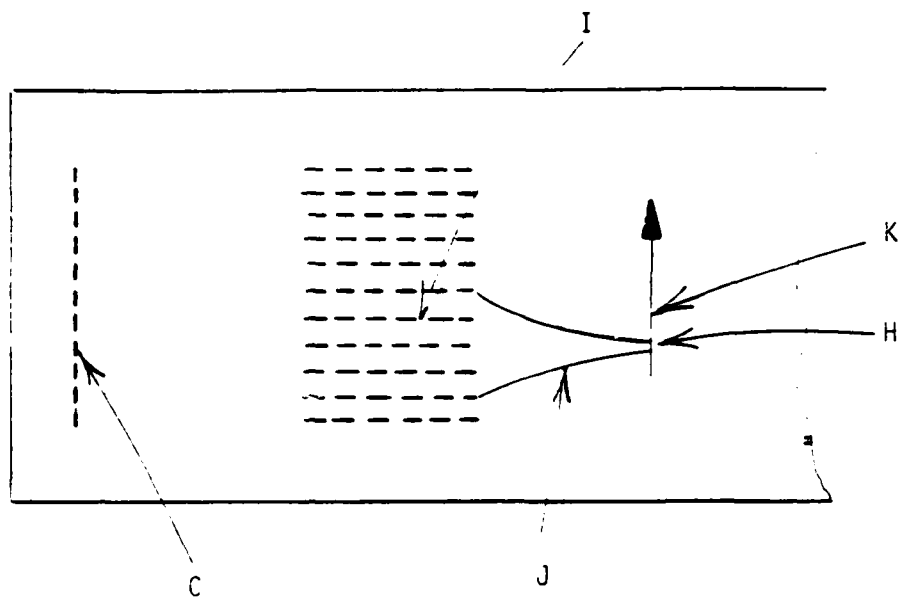
Fig. 7--Schematic of PVF<sub>2</sub> surface wave imaging device;  
(a) side view, (b) and (c) angled plan views.



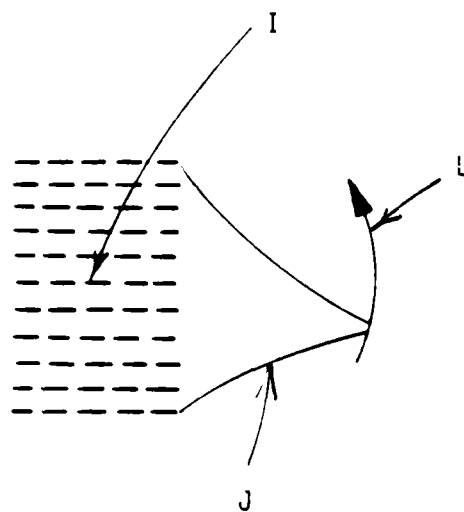
turn lead to a distribution of phases for the surface wave sources I (Fig. 7(c)) which then radiate cooperatively to produce a surface wave beam with wavefronts G (Fig. 7(b)), which converges toward a focal spot H. Note that the surface wave wavefronts G of Fig. 7(b) and (c) are not the same. The wavefronts in (b) result from a superposition of a number of wavefronts of the type shown in (c), which are individually phased to produce the converging beam shown in (b).

It would be realized from the above description that the proper phasing of the individual electrodes of the bulk wave array results in convergent focusing of the surface wave beam. We now point out that, in addition, further programming of these phases results in rapid electronic scanning of the surface wave beam, laterally across the surface of the substrate, in the focal "plane." This programming can be quite general, leading to different scanning patterns. Two examples are indicated schematically in Fig. 8. At (a) is shown a case in which a subset of the total set of sources radiates at any instant. The corresponding subset of bulk wave elements is excited with the phase profile required to form the converging beam J. By successively stepping this profile, one element spacing at a time, along the bulk wave array, the surface wave beam scans linearly along path K. In the example at (b), all sources radiate simultaneously. The phases of the individual elements can be programmed to produce any scan trajectory, such as the sector scan labelled L.

A summary of the analysis of the radiation from a linear array of transducers, which describes how a focused beam is produced and gives quantitatively the theoretical characteristics of the focused beam, is given in the Appendix.



(a)



(b)

J - FOCUSED SURFACE WAVE BEAM PROFILE  
 K - LINEAR ELECTRONIC SCAN LINE  
 L - SECTOR ELECTRONIC SCAN LINE

Fig. 8--Schematic scanning surface wave beam profiles.

#### D. Surface Wave Array Design and Construction

##### 1. Bulk Wave Portion

The bulk wave portion of the imaging array, parts A, B and C of Fig. 7, were fabricated using techniques developed here under another program sponsored by the Office of Naval Research, concerned with bulk wave transducers and bulk wave arrays using PVF<sub>2</sub>.<sup>12,13</sup> Since this is the starting point for the surface wave array, a description of the relevant parts of the bulk wave array work is included in this subsection.

Figure 9 is a schematic side view of this bulk portion of the array. The electroded elements are indicated in cross-section by the dashed lines, in the same manner as in Fig. 7(b). Note that the electrode elements in Fig. 9 are placed at the PVF<sub>2</sub>/backing interface. In principle they can be placed at either face of the PVF<sub>2</sub> film, and the choice is determined by practical considerations.

The individual electrode elements in Fig. 9 are defined by deposited thin film electrode strips which are indicated in cross-section by the dashed lines. They are deposited on a polished epoxy substrate using standard photolithographic techniques. This procedure avoids having to deposit the electrodes on the surface of the PVF<sub>2</sub> film itself. We chose this method because our state-of-the-art of high resolution deposition directly on PVF<sub>2</sub> film was not well developed at that time.

The uniform PVF<sub>2</sub> film is electroded on one side only, the (bottom side in Fig. 9) with an electrically grounded, uniform electrode. The non-electroded side of the film is placed in contact with the array pattern and epoxy bonded in place. We have shown in experiments with bulk wave transducers that there is no degradation of performance as a result of placing

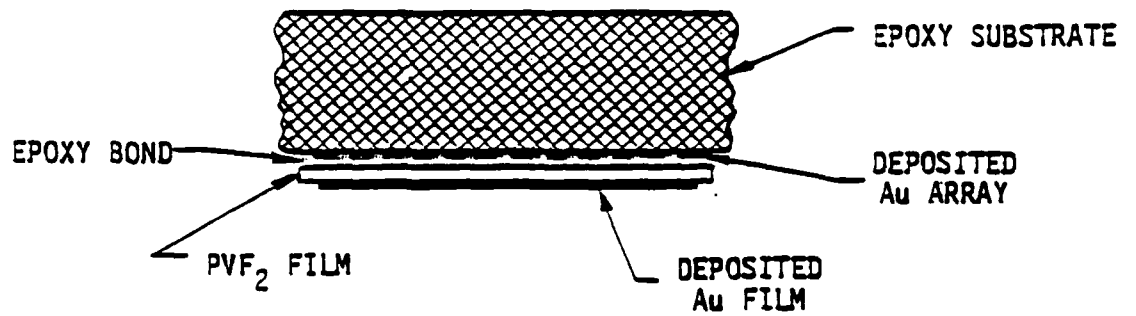


Fig. 9--Schematic cross-section of bulk wave portion of imaging array.

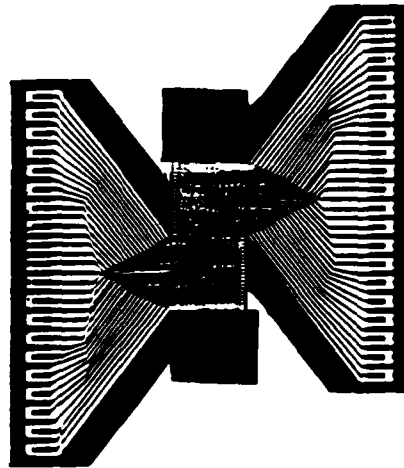


Fig. 10--Photo of electrode pattern.

the counter electrode on the substrate, where it is separated from the  $PVF_2$  by a thin layer of epoxy.

The substrate is a molded block of epoxy. Epoxy was chosen for several reasons. For one, the substrate cannot be a conductor if the array elements are to be deposited on it, since these elements must be operated at different potentials during imaging. The low acoustic impedance (3.2) of the epoxy is also advantageous. From earlier work we knew that a  $PVF_2$  transducer backed by a closely matched impedance will have an extremely large bandwidth.<sup>13</sup> This allows the array to be operated over a very wide frequency range, which extends far below the resonance frequency of the film (~ 40 MHz). The large bandwidth would also be advantageous if the array were operated in a pulsed mode. In that case, the matched backing would produce a very short, compact impulse response, allowing excellent axial resolution.

There are several key points to be made regarding the array design. First, no slotting operations between elements are required. PZT arrays are usually slotted in order to reduce acoustic and electrical cross coupling between elements. Both these kinds of cross coupling degrade the imaging properties of the array. Cross coupling causes errors in the rf signals applied to the electrodes. A focused beam formed by an array consisting of such coupled elements can have high side lobe levels and a larger beam spot size than for the uncoupled element case.

Slotting of a PZT slab plus matching layers is difficult and often can lead to nonuniform element response. Slight variations in the depth of the slot cuts will introduce these element-to-element differences. These variations will also harm the quality of the images produced by the array. They also make electrical tuning of the elements a slow, tedious process, since each element must be carefully tuned individually.

It is possible to avoid slotting the  $\text{PVF}_2$  array because acoustic cross coupling is inhibited by the low mechanical  $Q$  of the  $\text{PVF}_2$ .<sup>14</sup> Electrical cross coupling is not as severe in  $\text{PVF}_2$  as in PZT, because the low dielectric constant of  $\text{PVF}_2$  ( $8 \epsilon_0$ ) impedes electrical pick-up between elements. Electrical cross coupling is also suppressed in our design by including ground electrodes on the deposition mask. There is a ground electrode between each pair of active fingers.

Figure 10 is an enlarged photo of the photolithographic mask used to produce the finger pattern. We used the mask to produce electrodes which were parallel strips of  $1000 \text{ \AA}$  thick gold on top of a flash of chrome, fabricated by the liftoff photolithographic method. The finger widths and spacings are 5 mils, and the finger length is 9 mm. There are a total of 80 identical electrodes, 40 of which connect to electrically isolated bonding pads. The remaining 40 elements are directly joined to the ground electrode which surrounds the entire pattern.

A fan out from the active elements to the large bonding pads is included directly on the mask, so that microscopic bonding of the leads to the individual elements is completely avoided. Leads are easily soldered from the bonding pads to circuit boards within the array housing. From there, miniature coax cables travel to the controlling electronics.

The epoxy substrate is DER 332 resin with MPDA catalyst. It is  $4" \times 5" \times 1"$ , with one face having been lapped and polished before the electrode was deposited. The  $\text{PVF}_2$  film is 25 microns thick with a  $25 \text{ m} \times 12 \text{ mm}$  uniform electrode ( $50 \text{ \AA} \text{ Cr} + 1000 \text{ \AA} \text{ Au}$ ) on one side. The  $\text{PVF}_2$  film is epoxied onto the substrate at the center of the electrode pattern.

This construction procedure requires no critical alignments during fabrication. This applies to alignment of the electrode mask on the substrate, and to alignment of the  $PVF_2$  film, which can rotate or translate slightly during bonding without harm. Construction is simple to carry out, requiring only a few hours time.

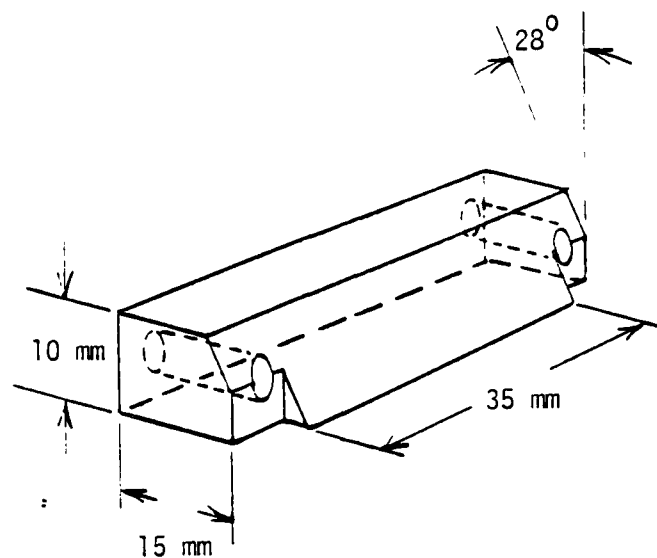
## 2. Surface Wave Portion

The surface wave portion of the array includes the wedge D and substrate F of Fig. 7.

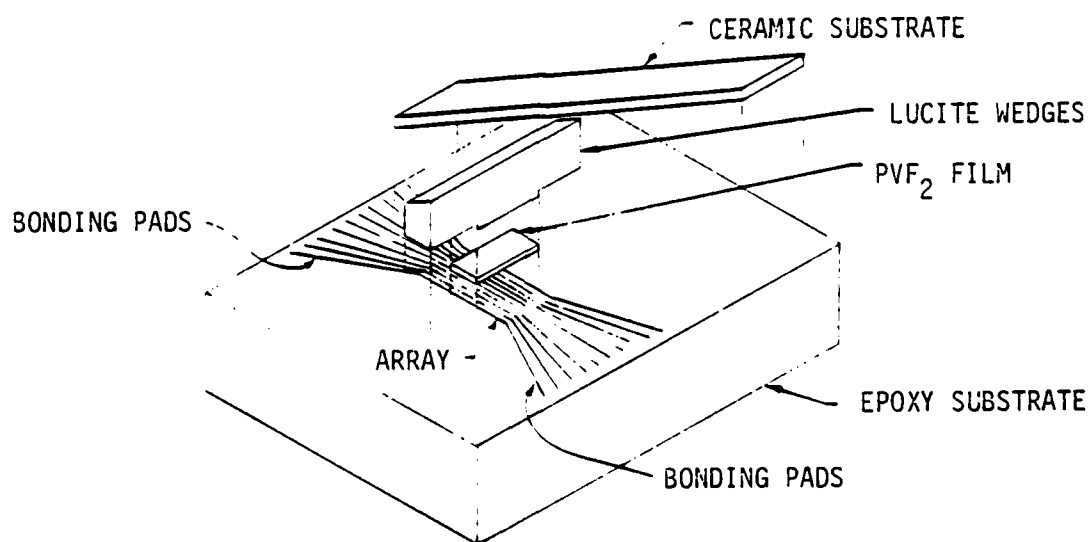
Because of the problems encountered in using our first generation wedge transducers, we sought a different wedge material (as opposed to RTV) when designing the  $PVF_2$  surface wave imaging array. Lucite is a good candidate for a coupling wedge. Its longitudinal acoustic impedance is 3.16 - an excellent match to  $PVF_2$  (3.82). Its acoustic longitudinal wave velocity is 2680 m/s. This results in a wedge angle of 28 degrees when coupling to silicon nitride. The optimum coupling length is  $14.6 \lambda$  or 9 mm at 5 MHz. Furthermore, lucite can be easily and accurately machined. This allowed us to securely fasten the wedge against the  $PVF_2$ , as will be seen.

The wedge length is also a reasonable value since the tolerance on the wedge angle is  $\Delta\theta < 1/(2N)$  where  $N$  equals the wedge length measured in acoustic wavelengths in the lucite. A  $\Delta\theta$  of  $1/(2N)$  results in a 3 dB decrease in coupling efficiency due to incomplete phase matching at the wedge-substrate interface. Thus if  $N$  becomes too large, the tolerance on the wedge angle shrinks prohibitively. Furthermore, the wedge angle lies in a reasonable range - it can be built without difficulty.

Figure 11(a) shows the geometry and dimensions of the wedge. One point to notice is that the "wedge" is not wedge shaped. Instead it is a wedge on



(a) Lucite wedge geometry.



(b) Schematic exploded view of assembly.

Fig. 11--Surface wave array.



top of a pedestal. This design was chosen over a plain wedge in order to increase the strength of the system. The figure shows that a significant amount of stress is being applied to the wedge, which itself is bolted to the epoxy substrate. A simple wedge (of angle = 10 degrees and length ~ 10 mm) is not sturdy enough to withstand much stress. Besides this factor, the plain wedge did not leave much room in which to hold the ceramic substrate to the lucite. For these reasons the extended wedge was employed. The wedge structure is wider than the bulk wave array, to allow it to be bolted to the epoxy substrate.

The overall assembly of the surface wave imaging array is indicated in Fig. 11(b). The bulk wave array, wedge and ceramic substrate are clamped together with a fixture as seen in the photo of Fig. 12. Figure 12 is upside down with respect to the Fig. 7; in Fig. 12 the bulk waves travel upward in the wedge, and surface waves are excited on the under side of the ceramic substrate, moving to the right.

At this point we might note some differences between bulk wave and surface wave imaging. The bulk wave portion of the device, when used for bulk wave imaging, is fitted with an acoustic cylindrical lens<sup>13</sup> which produces a focus in the direction parallel to the electrode strips of Fig. 9. This is because electronic focusing produces focusing only in the direction perpendicular to the strips, so that the lens is required to produce a focal spot of equal width in both directions. The strips are made much longer than their width, both to allow better electrical matching to low impedance sources, and to provide initial collimation of the acoustic beam in the direction parallel to the strips, which eases the lens design.

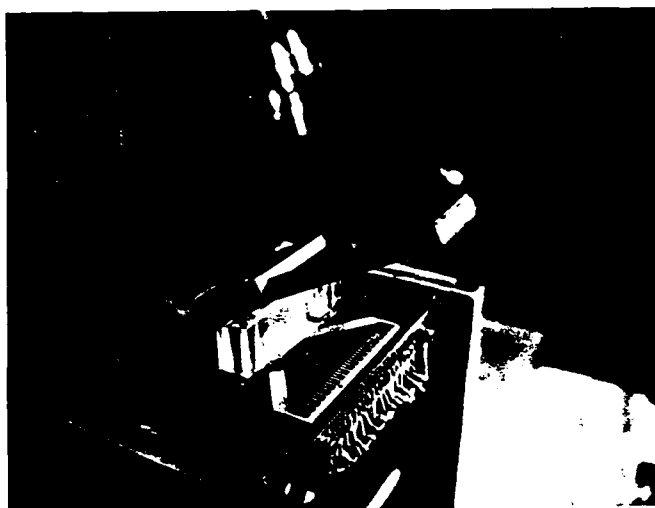


Fig. 12--Photograph of surface wave imaging system.

In the surface wave case of Figs. 7 and 11, the confinement of the surface wave to the vicinity of the substrate surface, by the surface waveguiding effect, eliminates the need for a cylindrical acoustic lens. This allows the focal length of the beam in Fig. 8 to be varied electronically so that, together with the electronic line scan of Fig. 8, one can do two-dimensional imaging over the face of the substrate electronically at high speed. In the bulk wave case, by contrast, the focal length is fixed by the cylindrical lens. Two dimensional imaging, in either a sagittal plane or the image plane, requires one mechanical scan (frame scan) when using a linear array.

#### E. Electronic System

An electronic system developed under other programs in this laboratory was made available to the present project for testing of the surface wave imaging array. A block diagram of the system is shown in Fig. 13. This system was designed and tested by K. Bates,<sup>15</sup> and has since been expanded, upgraded and used with a variety of imaging arrays by K. Fesler. A multi-level digital section, referred to as a digital delay line, allows the operator to choose the amplitudes and phases of the rf signals that are applied to each of 128 separate channels. The amplitudes and phases are controlled by a microcomputer. Only certain quantized values of phase and amplitude may be chosen. There are 16 available phase values, spaced by  $2\pi/16$  radians from each other. There are also 16 available amplitude levels. The largest provides an open circuit output of  $\sim 16$  volts, with the other values being linearly spaced from 15 volts down to 0 volts. The present PVF<sub>2</sub> array makes use of 40 of the 128 total channels.

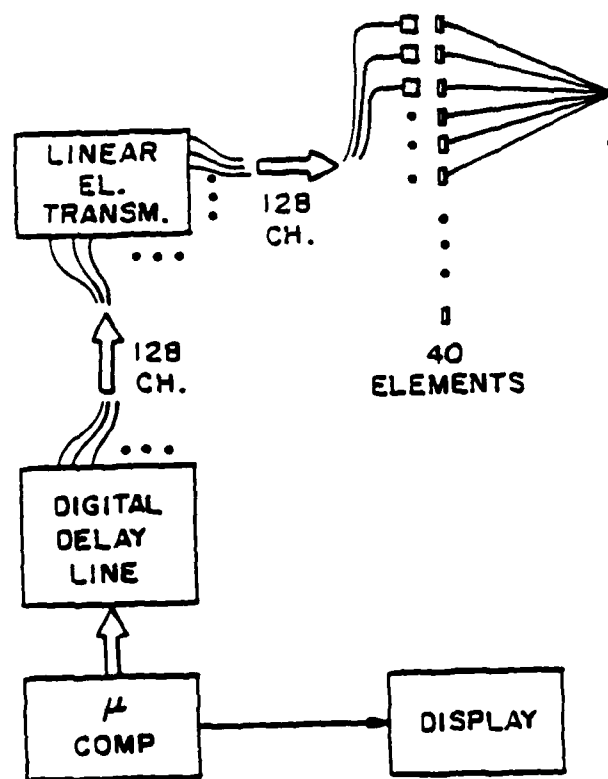


Fig. 13--Block diagram of electronic system.

#### F. Surface Wave Imaging Measurements on Silicon Nitride Samples

The imaging array (Fig. 12) was set up with miniature coax lines carrying rf signals from 40 of the channels of the electronic system (Fig. 13) to the bonding pads on the imaging array elements.

Our frequency of operation was 5 MHz. We were limited in our choice of frequency by the frequency range limitation of the electronic system. We wanted to use the highest possible frequency in order to increase the resolution of the system. Due to the design of the electronic section, 5 MHz was the maximum frequency possible.

Each element of the array will produce bulk waves in the lucite wedge as the elements are electronically driven. Because the width of the elements ( $\sim .125$  mm) is much less than the wavelength of the radiated bulk waves in the lucite ( $\sim .5$  mm) the waves will diffract and produce a wide beam pattern as they travel in the lucite (Fig. 7(c)). The wave fronts produced will impinge on the silicon nitride after traveling about 15 mm in the lucite. Those portions of the waves that intersect the  $\text{Si}_3\text{N}_4$  close to the phase matching angle of 28 degrees will successfully couple into surface waves. Energy of the wave that is not converted into surface waves goes into other modes, such as bulk waves reflected back into the lucite.

A focus is formed by phase delaying the signals to the individual elements. This means that the individual elements are not driven in phase with each other. While one element is driven by an electrical signal of the form  $\sin(\omega t)$ , another element will be driven by a signal of the form  $\sin(\omega t + \phi)$ , where  $\phi$  is a phase delay that is different for each element.

The correct phases to be applied to the elements were determined by calculating the distance from each individual element to the spot to be imaged. This is indicated schematically in Fig. 14, where the radial distances are imagined to include both bulk wave and surface wave portions of the wave paths. This distance of course was different for each separate element. Knowing the wavelength of the surface acoustic waves on the substrate allows one to compensate for the different travel distances between the elements and the image spot by driving each element with the appropriate phase signal such that the signals from all elements arrive at the image spot in phase.

The mathematics of phased array imaging is given in the Appendix. One important result derived in that section is that the focal spot size (and hence the resolution), is equal to  $\lambda \cdot f_n$ . Here  $\lambda$  is the wavelength of the surface waves and  $f_n$  is the f-number (inverse to numerical aperture) of the system. The f-number is equal to the distance from the focal spot to the array divided by the total array width (the distance between the two end elements of the array). Thus the smaller f-number of an imaging system, the better the resolution.

The array was operated in a linear scan mode in which 20 elements, out of the 40 total elements, were active at any instant. The scanning sequence consists of applying the proper distribution of rf signals to elements 1 through 20 at one end of the array, and then successively stepping this same distribution along to elements 2 through 21, 3 through 22, etc. In this way the beam moves along the scan line in 0.5 mm increments. At each step along the way the received signal is measured and stored in the computer.

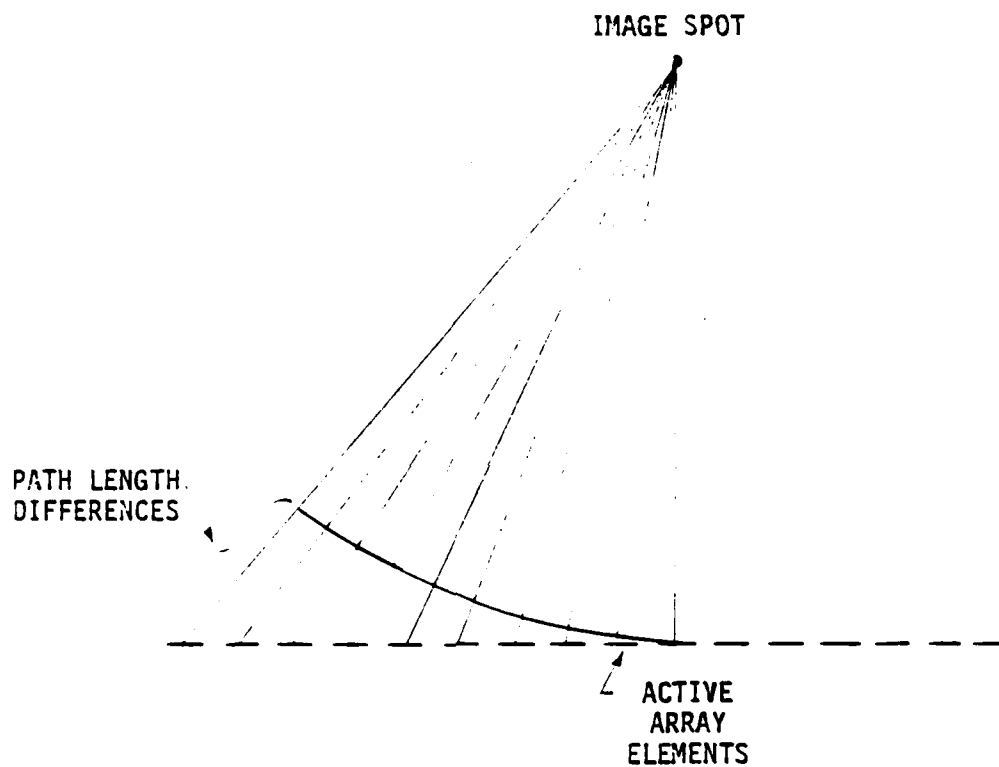


Fig. 14--Geometry of imaging. The path length difference from the elements to the image spot are compensated by applying electrical signals with different phases to the elements.

Linear scanning can be accomplished very quickly because of the simple nature of the method. Only 20 phases are needed to focus the beam (at a particular distance from the array). Once these phases are calculated they need only be shifted to the proper place within the computer so that the proper elements are excited. This shifting can be accomplished with great speed electronically. On the other hand, this method only uses half of the array elements at any one time. Therefore the f number of the system is twice as large as it might be, and the system resolution suffers.

Alternatively, all the elements can be used as radiators during the measurement of each data point (Fig. 8(b)). Thus the f number of the system is as small as possible. However, the phases which must be applied to the array elements are different for each scan point. Thus the phasing information must be calculated for each scan point. This can slow down the scan rate of the system. Because of its simplicity, we used a linear scan in all of our experiments.

The system was set up for transmission imaging, in which the focused beam from the array travels to a fixed strip receiving transducer located beyond the objects to be imaged. The beam geometry is given in Fig. 15, which is drawn to scale except that the array elements are indicated schematically, there being actually a total of 30 elements consisting of 40 active elements together with intervening ground electrodes.

#### 1. System Calibration

After construction of the surface wave imaging array had been completed, we performed some experiments that were designed to test the performance of the array. We wished to measure the imaging properties of the array, or in



TOP VIEW

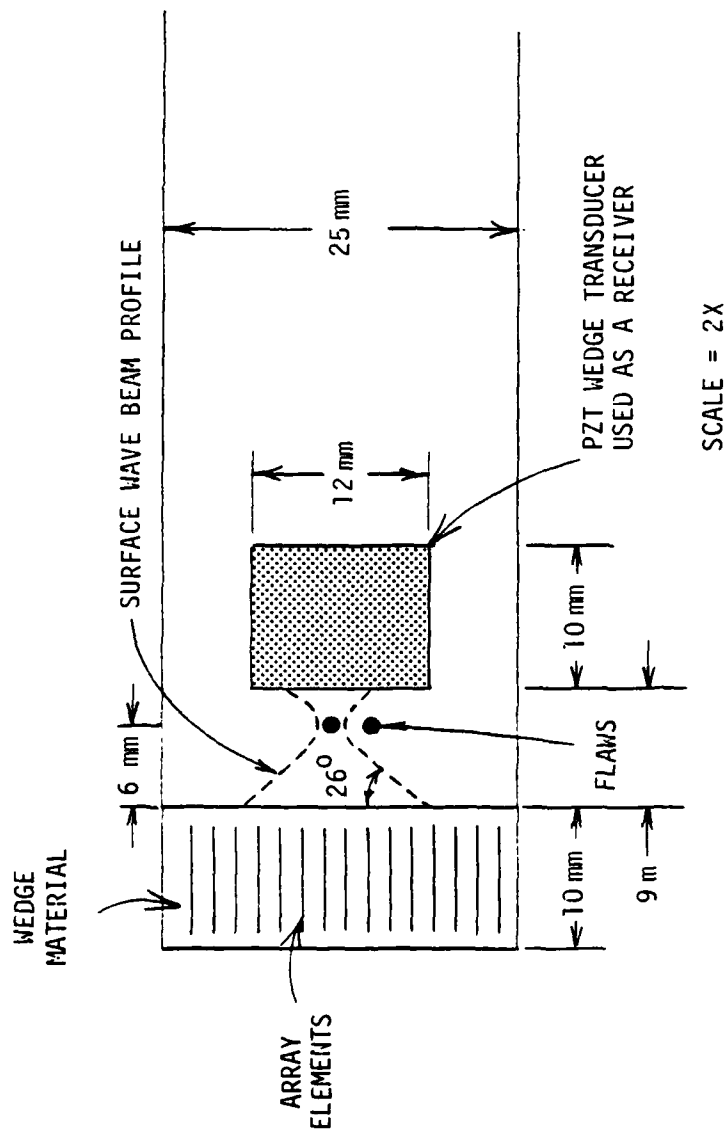


Fig. 15--Geometry of focused beam for f/1 aperture.

other words, to calibrate its performance. The two imaging properties whose quality we were most concerned with were the field of view of the imaging system and the resolution of the system.

The field of view of an imaging system refers to the area which lies within the range of the imaging system. In the case of our array, we want to consider the field of view at a fixed focal length. Thus, the field of view will be a length of territory located on the substrate running parallel to the scanning direction of the beam.

In an ideal situation the field of view would extend from one end of the substrate to the other. Furthermore, in the ideal case the amplitude of the focused acoustic beam would be uniform, absolutely flat, across the scan line. Here we will consider both the extent of the field of view and the uniformity of the system across the field.

In practice, our field of view was not ideal due to several factors. One factor was the length of the array. As mentioned before, we used a linear scan. This method cannot scan to the edges of the array because the array elements do not extend far enough to allow the complete focused acoustic beam to reach the substrate edges. The finite extent of the array limits the main field of view to 10 mm. The array can scan beyond either end of the 10 mm field of view, but when this occurs less than 20 array elements contribute to the acoustic beam. Therefore the beam strength slowly tapers off and the resolution decreases outside of this range.

Another factor limiting the field of view of the entire system was the aperture of the receiving transducer. This aperture (12 mm wide) was only slightly larger than the 10 mm field of view. The focused acoustic beam itself had a width of up to several millimeters, depending on the scan conditions at the receiver position, i.e., beyond the focal point.

Thus the focused beam may not have been totally incident on the receiver during some portions of a scan, i.e., parts of the beam may not have been detected by the receiver at the two ends of the 10 mm scan length. This effect also causes a rounding off of the ends of the scanning length response.

The alignment of the receiver relative to the transmitter also can change the uniformity of the scan. In order to obtain good, reproducible results the receiving transducer must be securely clamped to the substrate. It must be carefully rotated so that it is properly aligned with respect to the array.

The uniformity of the beam across the field of view can also be a function of the uniformity of the transducers of the system. There was no easy way to measure the transducer uniformity. The effects of non-uniformities of the individual transducers are hidden in the overall system response.

We measured the extent and uniformity of the field of view by scanning the system across an unflawed portion of the substrate. Figure 16 shows the results of the measurements. We see a relatively flat plateau of about 7 mm which slowly and smoothly falls off to zero over several millimeters. Thus the field of view of the system was relatively small, but was fairly uniform.

The next calibration test was the measurement of the point response of the array. This measurement is a good indication of the system resolution. As mentioned earlier, the calculated beam width (defined here as the full width at half the maximum power is  $\lambda \cdot f(n)$  .

The measurement was performed by scanning the focused beam past a small aperture receiver. We used a 2 mm wide PZT wedge transducer (with a lucite

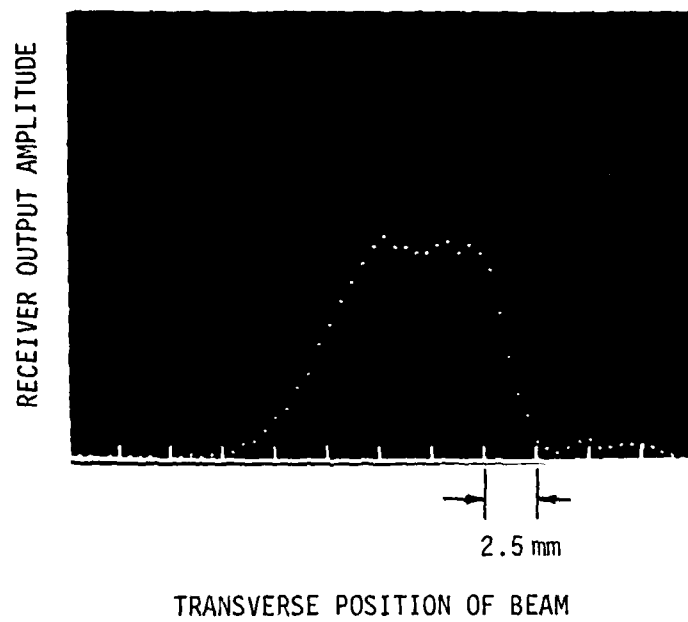


Fig. 16--Imaging system field of view.

wedge) as the receiver. The point spread function was measured with the beam focused close to the receiver at a distance of 12 mm from the array. The result is shown on Fig. 17, which plots the relative output voltage amplitude of a linear detector. The measured width of the main lobe at the half power points is 2 mm. Theory predicts a width of  $\sim 1.4$  mm. The near-in side lobe level is  $\sim -15$  dB, as compared to  $-13$  dB theoretical for a rectangular aperture array.

The difference between the measured and theoretical beam widths results partly from the fact that the measurement is made with a receiver aperture whose width is larger than the beam width. By deconvolving the measured beam width and the receiver aperture width the experimental value for the actual beam width becomes less than 2 mm, while the theoretical value is 1.4. The slight advantage in side lobe suppression over the theoretical value can result from inherent apodization effects associated with the angle response functions of the individual surface wave "sources" (Fig. 7(c)). Additionally, with regard to comparison between theory and practice in general, the theory considers radiators of negligible depth in the direction parallel to the beam direction. This was not true for the surface wave array. As can be seen on Fig. 7(c), the surface wave "source" array extends for 9 mm. This is not a negligible distance considering that we were using focal lengths of 12 mm. We have not yet evaluated the effect of this factor quantitatively.

## 2. Imaging Experiments

The measurement of the point spread function and field of view was one step in the evaluation of the surface imaging array. Our next step was to actually image some simulated surface defects. This was not an

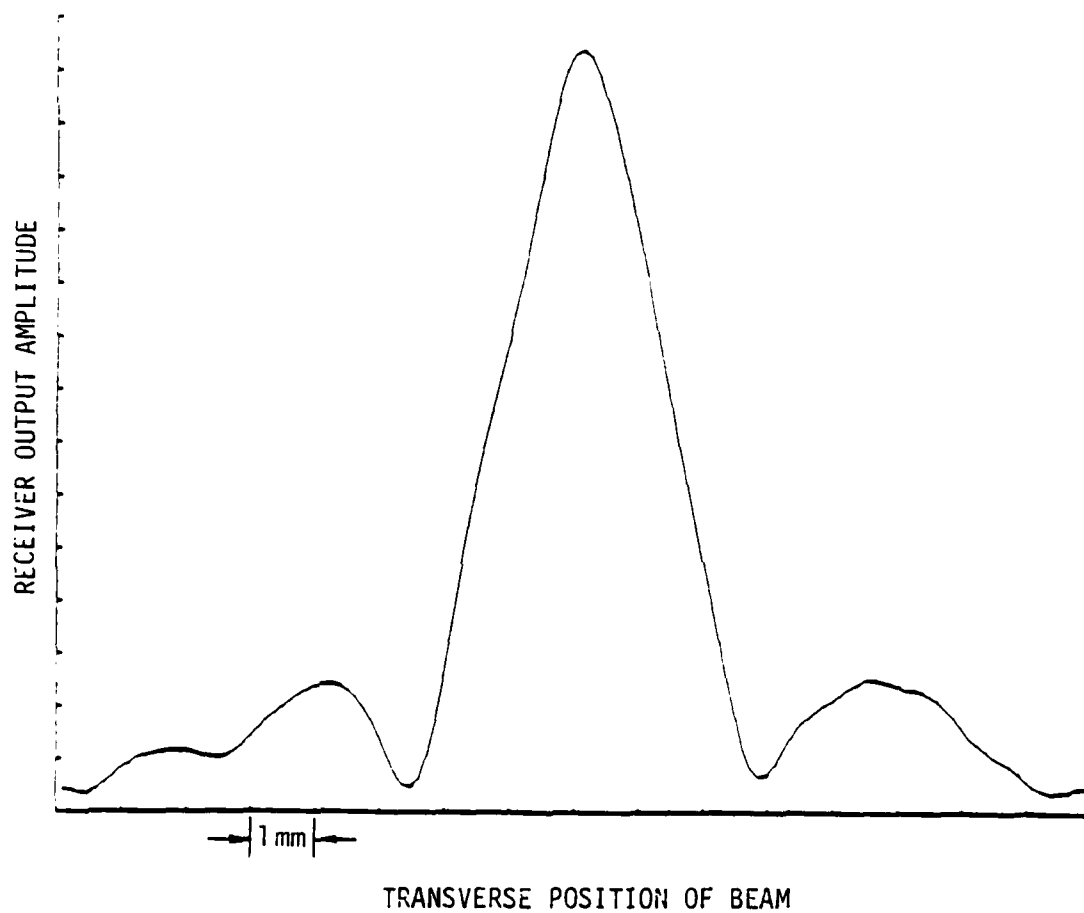


Fig. 17--Measured point response of imaging array at 12 mm focal distance.

attempt to perform a nondestructive test measurement, but rather an initial test of the imaging properties of the system. This process provides a more comprehensive measure of the imaging properties of the system than the calibration measurements. It provides data on the basic speed and accuracy of the overall scanning system.

For this purpose we simulated surface flaws by drilling two holes into the previously uniform and polished surface of a silicon nitride test plate. The holes were 1.5 mm in diameter, .5 mm deep, and were positioned so that the centers of the holes were 3.0 mm apart. The flaws were placed on the substrate surface so that the line connecting their centers was parallel to the scan direction of the array. They are shown to scale in Fig. 15.

The overall plan of the experiment was to electronically scan the substrate surface not just from side-to-side, but also from back to front by changing the beam focal length. By analyzing the data obtained we hoped to obtain initial data on the resolving power of the system resolution, verify that the focal length could be electronically controlled, and study the acoustic beam parameters.

The experimental procedure was as follows. The flaws were positioned 6 mm from the edge of the lucite transmitting wedge. The acoustic beam was focused at several different distances and scanned laterally across the substrate at these distances. The electrical output of the receiving transducer was digitized and stored. Each scan consisted of 32 discrete points. Next, the data were interpolated so that the original 32 points were increased to 128, for curve smoothing. Interpolation was accomplished by convolving the original data with a discrete sinc function that preserved the Fourier spectrum of the data. Figures 18 through 22 show five of the scans thus obtained.

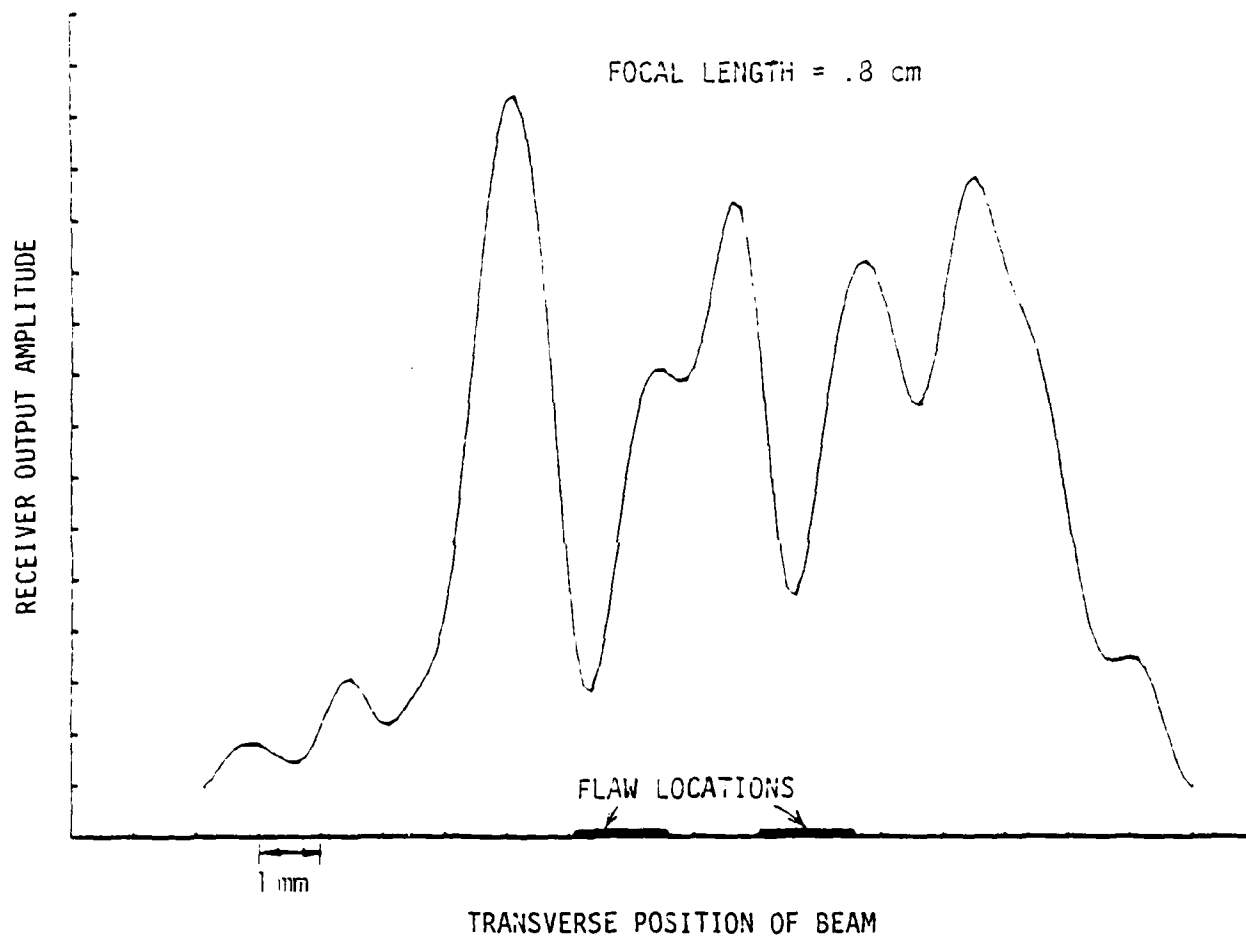


Fig. 18--Linear transverse line scan at fixed focal length.



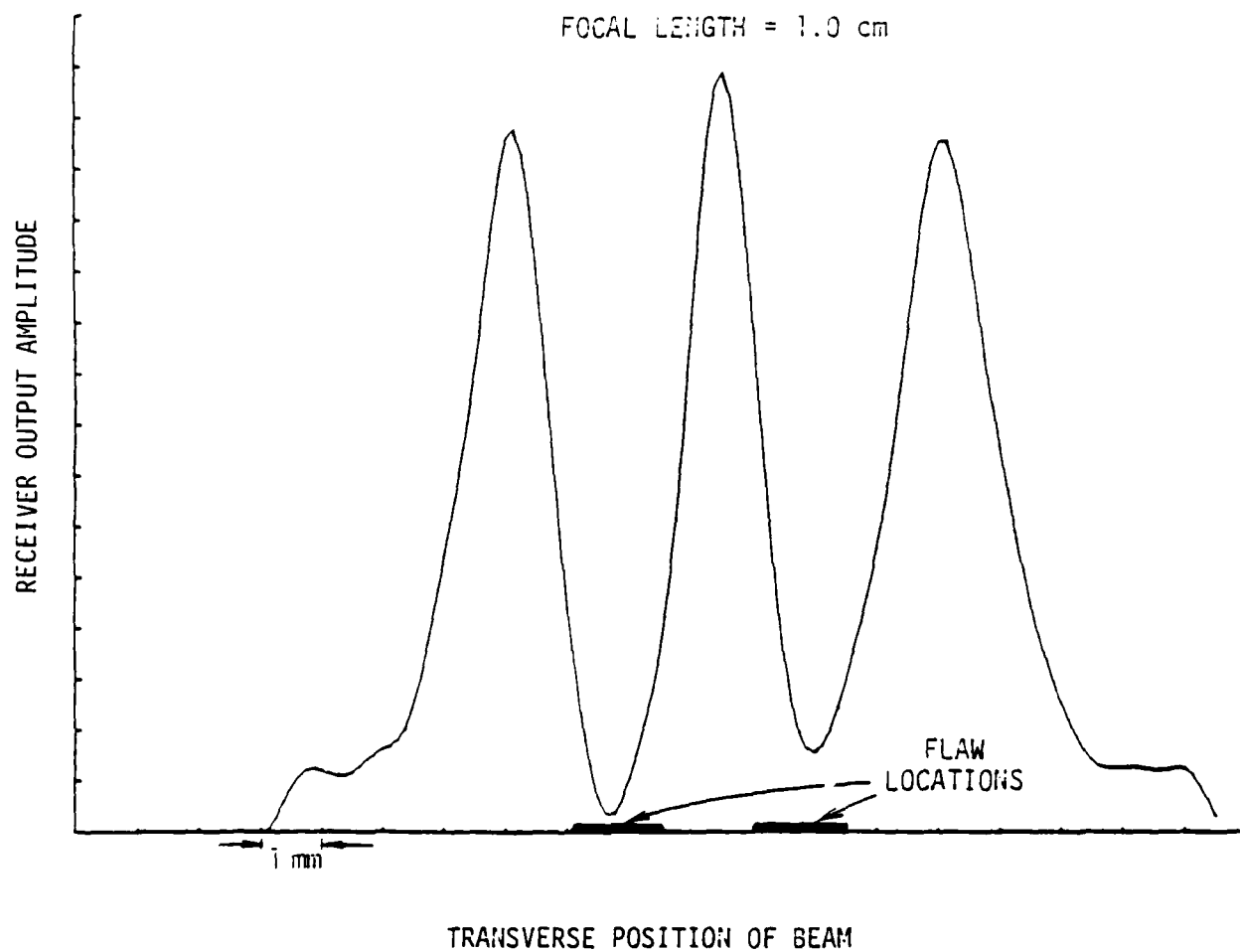


Fig. 19--Linear transverse line scan at fixed focal length.

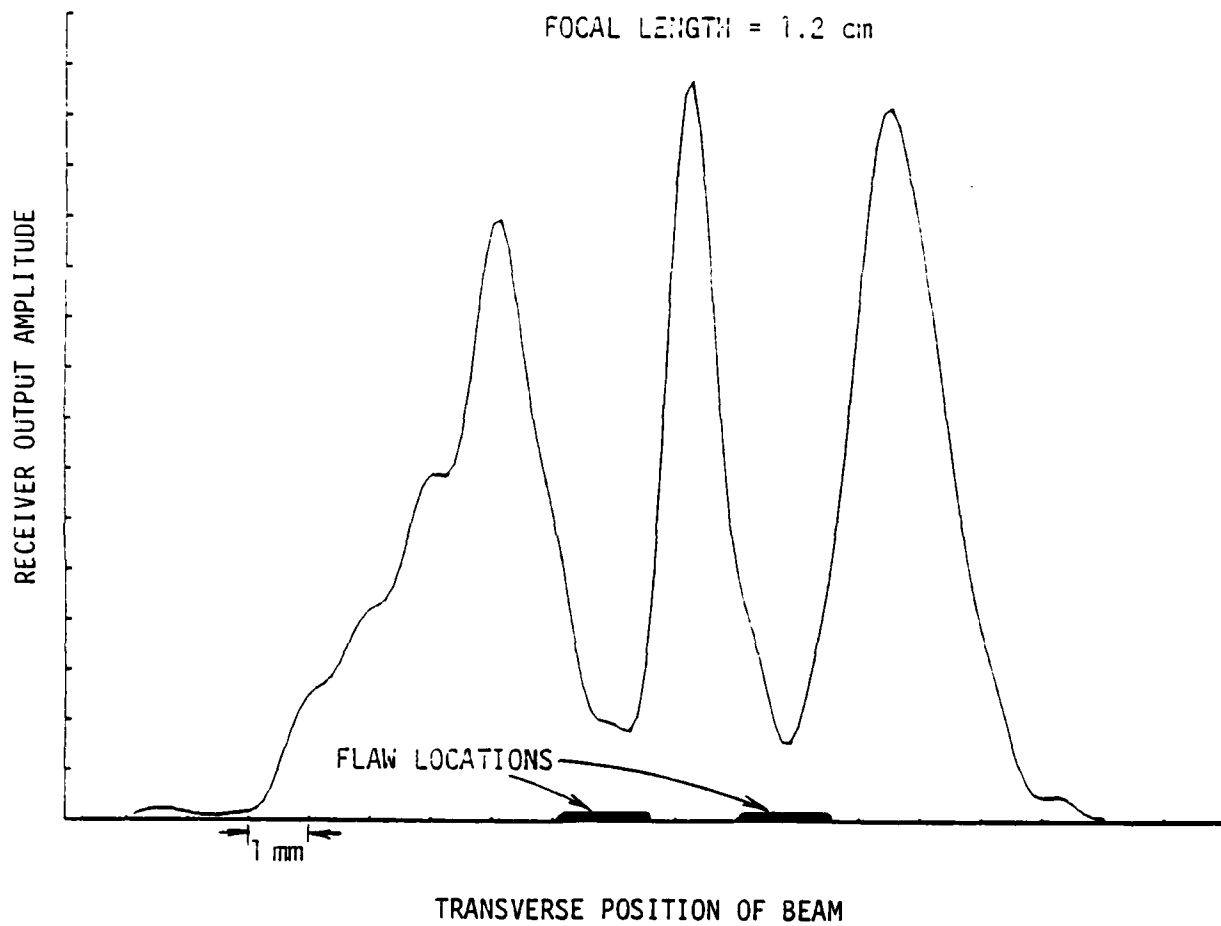


Fig. 20--Linear transverse line scan at fixed focal length.

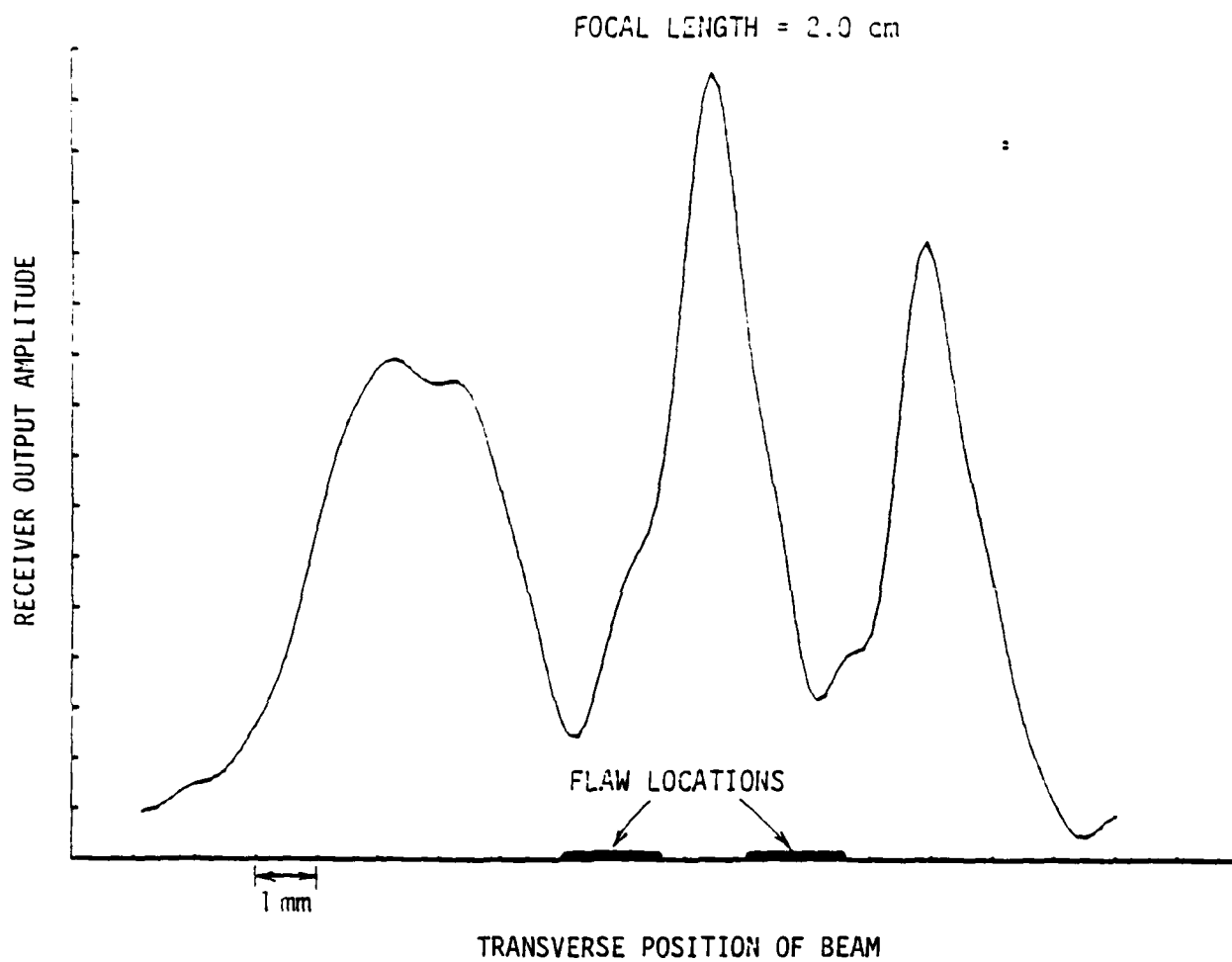


Fig. 21--Linear transverse line scan at fixed focal length.

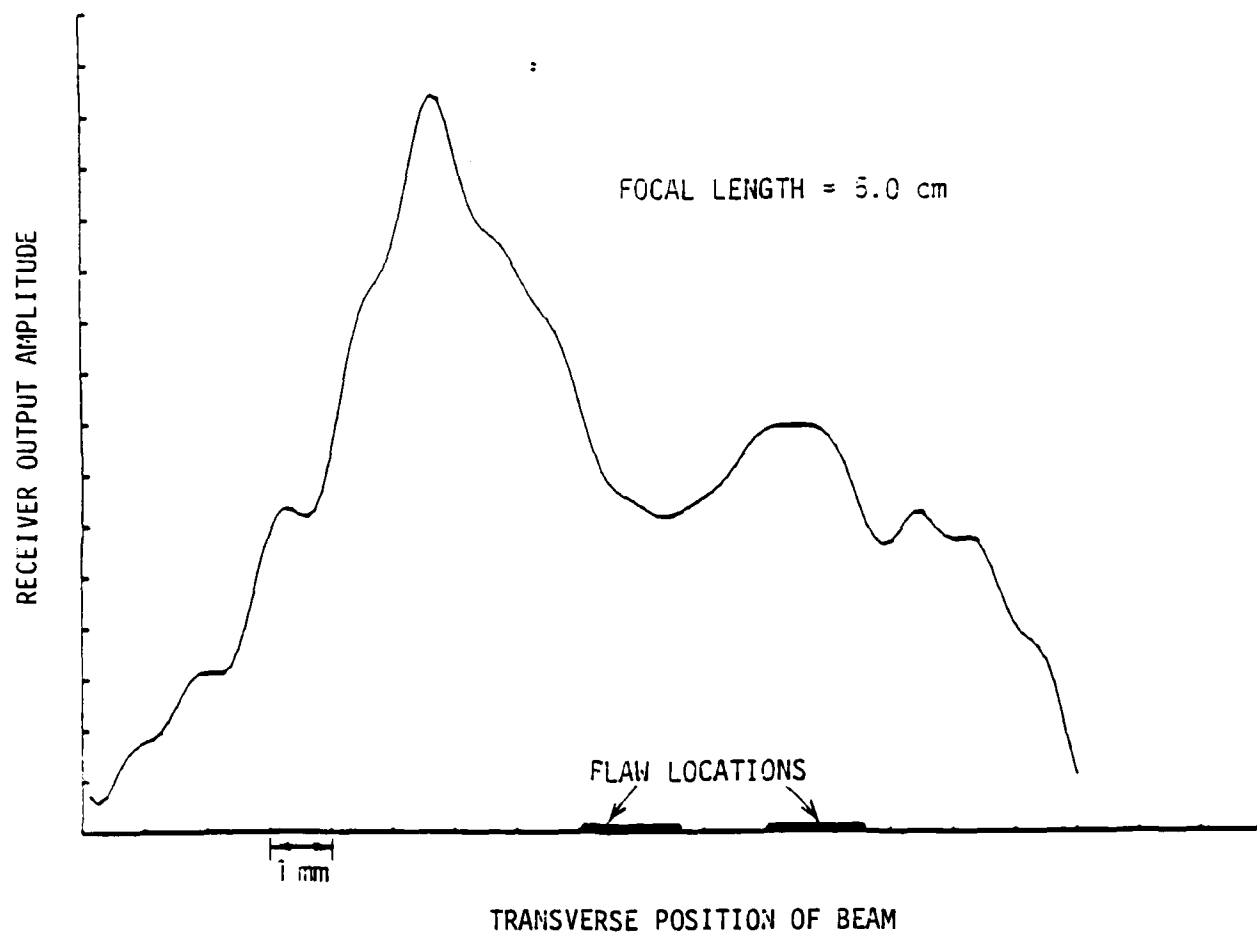


Fig. 22--Linear transverse line scan at fixed focal length.

As listed on the figures, these scans had focal lengths of .8, 1.0, 1.2, 2.0, and 5.0 cm. We define these focal lengths as distances measured from the lateral center line of the surface wave sources of Fig. 7(c). The phase distributions applied to the electrodes of the bulk wave array were chosen to give, theoretically, the above set of focal lengths.

The locations of the flaws are indicated on the figures. It will be seen that the valleys occur in the received amplitude at the locations of the flaws. Deep valleys correspond to high image contrast. The scans with focal length equal to 1.0 and 1.2 cm are the best scans in the sense that the contrast between the peaks and valleys of the curves is greatest for these two scans, as expected.

As the focal length is moved away from the 1.0 cm range the contrast of the scans falls off, also as expected. We see that the  $f = 2.0$  cm scan has a slightly lower contrast than the best scans. However, the presence and location of the defects are clearly signaled. The  $f = 5.0$  cm result reveals the flaws, but with the lowest contrast of any of the results. The scan performed with  $f = .8$  cm has good contrast, but also contains an artifact indicating the presence of a flaw where there is none.

The system clearly resolved the two flaws which were separated by 1.5 mm, and thus the resolution of the entire system is better than this value. This result is in agreement with the calculated resolution of 1.4 mm.

Several general comments may be made concerning the results presented here. To begin, all the scans successfully found the flaw positions. The system was successfully operated with a highly convergent beam with very low  $f$ -number of  $f/1$ . Also, the contrast followed the expected trend in which scans with  $f$  near 1.0 cm were of high contrast, while the contrast

declined as the focal length was moved away from this range. Finally, the scans at the extreme focal lengths also contained detail which did not correspond to real flaws.

Our results demonstrate that the transmitted beam does indeed come to a focus, and that the focal length can be electronically altered without difficulty. The changing contrast levels can be coordinated with the distance to the flaws being scanned. Also, the lateral position of the test flaws is clearly revealed by the beam scans. Thus, a two-dimensional map of the substrate surface can be produced by scanning laterally across the substrate at many different focal lengths.

It will be realized that the field of view in this process is limited only by the apertures (transverse lengths) of the transmitting array and the receiving strip transducer. Extension of both of these lengths would be straightforward. With regard to the array, additional elements could be added at will to increase the length without bringing grating lobes into the field of view. It is found that the one-dimensional fan-out of the electrodes to the bonding pads (Fig. 10) can be replaced by a two-dimensional stagger pattern that would allow unlimited increase in the number of elements in the active array.

### 3. Summary and Predictions

An experimental system using  $\text{PVF}_2$  piezoelectric film as the active element has been demonstrated which provides electronically-controlled, high speed two-dimensional ultrasonic imaging on the surface of a ceramic sample. Scanning bulk waves are converted to surface waves at the ceramic surface. The system produces an electronically focused, highly convergent surface wave beam with an  $f/1$  aperture, with variable focal length and

capable of arbitrary scanning patterns by changing the phase distribution of rf signals applied to a linear array of electrodes via a microcomputer. Simulated flaws on the surface were used in an initial investigation of the beam shape and imaging characteristics, which are found to be consistent with theoretical predictions. Using a frequency of 5 MHz, a resolution in the range of 1.5 to 2 mm is observed. The field of view of 10 cm in the present system could be increased to larger values by straightforward extensions of the present design.

The  $\text{PVF}_2$  transducer array is easily, quickly and inexpensively fabricated using standard photolithographic techniques. The system uses a scanning transmitter array and nonscanning receiving transducer: substitution of a second, identical array as receiver would also be straightforward, to produce a unique double-scanning surface wave system with higher resolving power, dynamic range, and discrimination against artifacts. The  $\text{PVF}_2$  film is capable of operation at much higher frequencies, for higher resolving power, which could be exploited using a higher-frequency electronics section. In other possible future extensions, the natural mechanical flexibility of the  $\text{PVF}_2$  film could be used, together with flexible wedges, to produce similar surface wave imaging on curved surfaces.

## REFERENCES

1. Annual Report for Grant AFOSR-77-3386 for the period July 1, 1977 through June 30, 1978, Edward L. Ginzton Laboratory Report No. 2903 Stanford University (January 1979).
2. Annual Report for Grant AFOSR-77-3386 for the period July 1, 1977 through June 30, 1978, Edward L. Ginzton Laboratory Report No. 2903 Stanford University (January 1979), and Annual Report for Grant AFOSR-77-3386 for the period July 1, 1978 through June 30, 1979, Edward L. Ginzton Laboratory Report No. 3109, Stanford University (March 1980).
3. J. Kwai, J. Appl. Phys. 8, p. 975 (1969).
4. J. Ohigashi, J. of Appl. Phys, 47, 3, p. 949-955 (March 1976).
5. T. Waugh and G. S. Kino, Acoustical Holography 7, Plenum Publishing Corp., New York (1977), p. 103.
6. J. Linvill, Stanford Electronics Laboratories Report No. 4834-3, p. 71 (1978).
7. E. Carome, H. J. Shaw, D. Weinstein and L. Zitelli, 1979 Ultrasonics Symposium Proceedings, p. 346.
8. H. Sussner, et al., Phys. Lett. 45A, p. 475 (1973).
9. H. Fraser, B. T. Khuri-Yakub, and G. Kino, Appl. Phys. Lett. 32, 11, 698 (June 1, 1978).
10. J. Fraser, Ph.D. Thesis, Edward L. Ginzton Laboratory Report No. 2973, Stanford University, p. 46-59 (May 1979).
11. E. Carome, K. Fesler, H. J. Shaw, D. Weinstein, and L. Zitelli, 1979 Ultrasonics Symposium Proceedings, p. 641.
12. Final Report for Contract N00014-77-C-0582 for the period August 1, 1977 through January 31, 1981.



13. H. J. Shaw, D. Weinstein, L. Zitelli, C. W. Frank, R. C. DeMattei, and K. A. Fesler, 1980 Ultrasonics Symposium Proceedings, p. 927.
14. P. Horvat, J. Gagnepain, and B. Auld, 1979 Ultrasonics Symposium Proceedings, p. 511-514.
15. K. Bates, E. Carome, K. Fesler, R. Liu, and H. J. Shaw, 1979 Ultrasonics Symposium Proceedings, p. 216-219.

## Appendix

### Radiation from a One-Dimensional Transducer Array

Consider a one-dimensional array of acoustic transducers as shown in Fig. A.1. The center-to-center spacing of the elements =  $d$ , the element width =  $\ell$ , the total number of elements =  $N$ , and the total length, or aperture, of the array =  $Nd = D$ .

Across the face of the array acoustic waves will be emitted. The magnitude and phase of these waves will vary with position, and can be described by the function  $U(x)$ . We wish to determine the field developed by the radiating array at a line a distance  $z$  from the array.

Starting from Huygen's principle it can be shown that the field developed at the object line is

$$U(x_1) = \frac{1}{j\lambda} \int U(x) \frac{e^{jkr}}{r} dx \quad (\text{A.1})$$

where  $\lambda$  is the wavelength of the acoustic waves and  $r$  is as shown in Fig. A1.

The distance from the source points to the field points is  $r$ , and

$$r = [z^2 + (x-x_1)^2]^{1/2} \quad (\text{A.2})$$

We now make the usual paraxial approximation, assuming that  $z \gg (x-x_1)$  and say

$$r \sim z + \frac{(x-x_1)^2}{2z} \quad (\text{A.3})$$

We also replace the  $r$  in the denominator of equation (A.1) by  $z$ ,

Then we have

$$U(x_1) = \frac{e^{jkz}}{j\lambda z} + \frac{j k x_1^2}{2z} \int U(x) e^{\frac{j k x^2}{2z}} e^{-j k x x_1 / z} dx \quad (\text{A.4})$$

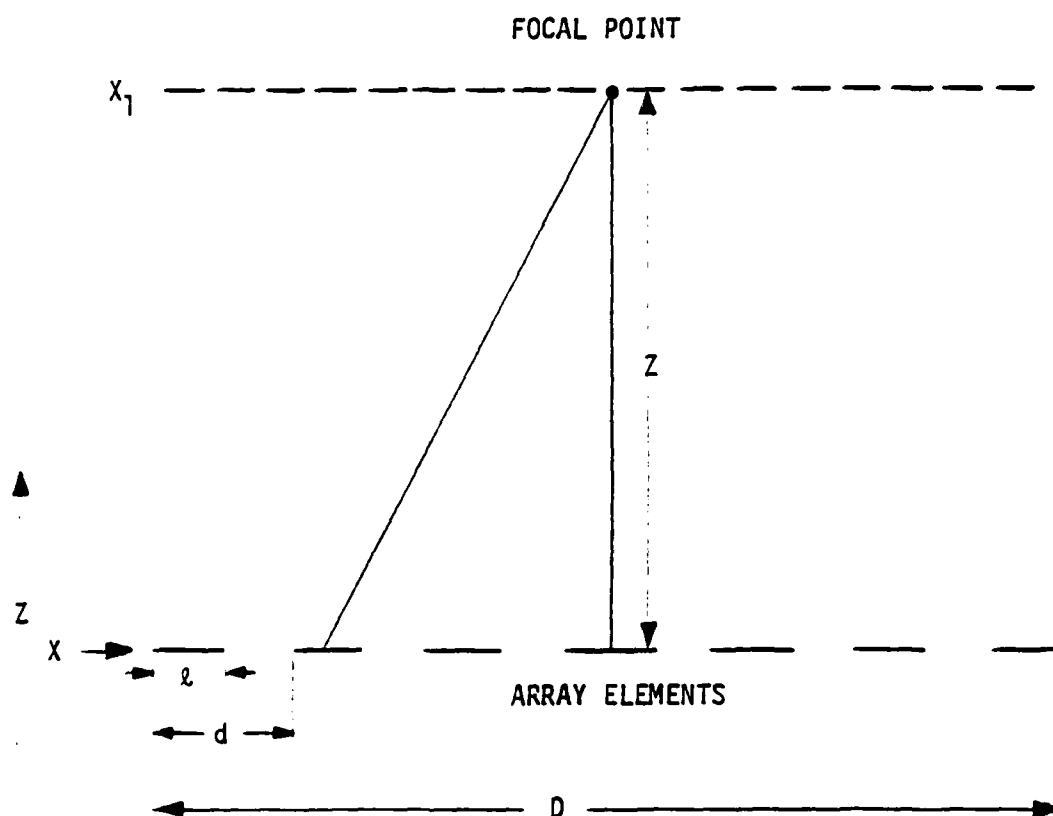


Fig. A.1--Imaging geometry.

In many imaging systems, including ours,  $U(x)$  is manipulated so that the term  $\exp[jkx^2/2z]$  that appears in the integral of equation (A.4) is nullified. This is accomplished by the focussing mechanism of the system. Then the integral is in the form of a Fourier transform. The result is that

$$|U(x_1)| = \frac{1}{\lambda^2 z^2} \int t(x) e^{-jkxx_1/z} dz \quad (A.5)$$

where  $t(x)$  is the transducer shape, in this case, an array of rectangle functions,

$$t(x) = \text{rect}\left(\frac{x}{D}\right) \text{rect}\left(\frac{x}{d}\right) * \text{comb}\left(\frac{x}{d}\right) \quad (A.6)$$

The output field is the Fourier transform of  $t(x)$ .

This can be shown to be

$$U(x_1) = \sum_{n=-\infty}^{\infty} \text{sinc}\left(\frac{n\lambda}{d}\right) \text{sinc}\left(\frac{Dx_1}{\lambda z} - \frac{nD}{d}\right) \quad (A.7)$$

There are two main types of imperfections in this response as compared to a perfect impulse response. There are sidelobes present on the  $\rightarrow \text{sinc}\left(\frac{Dx_1}{\lambda z} - \frac{nD}{d}\right)$  term. These have a full width at their -4 db points when

$$\frac{Dx_1}{\lambda z} = 1 \quad \text{or} \quad \Delta x_1 = \frac{\lambda z}{D} = \lambda f_n \quad (A.8)$$

where  $f_n$ , the f number, is defined as  $z/D$ .

Also present are grating lobes which appear due to the discreteness of the array. These grating lobes are spaced in the x direction by a distance

$$\Delta x = \frac{\lambda z}{d} \quad (A.9)$$

Due to the earlier paraxial assumption, equation (A.9) is only valid if  $x \ll z$ . The grating lobes can actually be eliminated by moving them beyond the

horizon seen by the array. For a system focussed directly ahead of the array, choosing  $\lambda > d$  will eliminate the grating lobes. If the array focus is being swept across the field of view the grating lobes will be eliminated when  $d < \lambda/2$ .